


METHODOLOGY

Open Access



Rapid, accurate computation of narrow-band sky radiance in the 940 nm gas absorption region using the correlated k -distribution method for sun-photometer observations

Masahiro Momoi^{1*} , Hitoshi Irie¹, Miho Sekiguchi², Teruyuki Nakajima³, Hideaki Takenaka¹, Kazuhiko Miura^{4,5} and Kazuma Aoki⁶

Abstract

We developed lookup tables for the correlated k -distribution (CKD) method in the 940 nm water vapor absorption region (WV-CKD), with the aim of rapid and accurate computation of narrow-band radiation around 940 nm ($10,000\text{--}10,900\text{ cm}^{-1}$) for ground-based angular-scanning radiometer data analysis. Tables were constructed at three spectral resolutions ($2, 5, \text{ and } 10\text{ cm}^{-1}$) with quadrature values (point and weight) and numbers optimized using simulated sky radiances at ground level, which had accuracies of $\leq 0.5\%$ for sub-bands of 10 cm^{-1} . Although high-resolution WV-CKD requires numerous quadrature points, the number of executions of the radiative transfer model is reduced to approximately 1/46 of the number used in the line-by-line approach by our WV-CKD with a resolution of 2 cm^{-1} . Furthermore, we confirmed through several simulations that WV-CKD could be used to compute radiances with various vertical profiles. The accuracy of convolved direct solar irradiance and diffuse radiance at a full width at half maximum (FWHM) of 10 nm, computed with the WV-CKD, is $< 0.3\%$. In contrast, the accuracy of convolved normalized radiance, which is the ratio of diffuse radiance to direct solar irradiance, at an FWHM of 10 nm computed with the WV-CKD is $< 0.11\%$. This accuracy is lower than the observational uncertainty of a ground-based angular-scanning radiometer (approximately 0.5%). Finally, we applied the SKYMAP and DSRAD algorithms (Momoi et al. in Atmos Meas Tech 13:2635–2658, 2020. <https://doi.org/10.5194/amt-13-2635-2020>) to SKYNET observations (Chiba, Japan) and compared the results with microwave radiometer values. The precipitable water vapor (PWV) derived with the WV-CKD showed better agreement (correlation coefficient $\gamma = 0.995$, slope = 1.002) with observations than PWV derived with the previous CKD table (correlation coefficient $\gamma = 0.984$, slope = 0.926) by Momoi et al. (Momoi et al., Atmos Meas Tech 13:2635–2658, 2020). Through application of the WV-CKD to actual data analysis, we found that an accurate CKD table is essential for estimating PWV from sky-radiometer observations.

Keywords: Atmospheric gas absorption, Correlated k -distribution, Radiative transfer

1 Introduction

Aerosols, clouds, ozone, and water vapor are important parameters for characterizing Earth's climate and changes therein (e.g., IPCC 2021) and are therefore considered essential climate variables by the World Meteorological Organization (Bojinski et al. 2014). Some of these parameters are measured using ground- and satellite-based instruments and estimated using the multi-term

*Correspondence: m.momoi@biglobe.jp

¹ Center for Environmental Remote Sensing, Chiba University, 1-33 Yayoicho, Inage-ku, Chiba 263-8522, Japan

Full list of author information is available at the end of the article

least squares method (e.g., Dubovik and King 2000; Rogers 2000), with radiative transfer models (RTMs) as the forward model. For example, Kudo et al. (2021) simultaneously estimated aerosol microphysical and optical properties, as well as ozone and water vapor column concentrations, using the angular distributions of diffuse radiance observed with an angular-scanning radiometer (e.g., Holben et al. 1998; Nakajima et al. 2020) proceed with the SKYRAD.pack MRI version 2.

The computational efficiency of the radiance calculation can be improved through use of the lookup table (LUT) method, rather than direct application of the RTM, as the forward model. However, the recent trend in aerosol remote sensing with ground- and satellite-based radiometers (e.g., Dubovik et al. 2011; Nakajima et al. 2020; Sinyuk et al. 2020; Kudo et al. 2021) has been toward increasing the number of retrieved parameters, and direct use of RTMs is preferred for analysis of ground-based angular-scanning radiometer data with high degrees of freedom for control variables. Several RTMs have been used for analysis of ground-based remote sensing data. For example, the AEROSOL ROBOTIC NETWORK (AERONET; Holben et al. 1998), which is an international network of ground-based angular-scanning radiometers, uses a scalar RTM called RSTAR (System for Transfer of Atmospheric Radiation for Radiance calculations; Nakajima and Tanaka 1986, 1988) in version 2 of its inversion algorithm (Dubovik and King 2000; Dubovik et al. 2000, 2006), and a vector RTM called SORD (Successive ORDERS of scattering; Korokin et al. 2017) in version 3 (Sinyuk et al. 2020). The SKYNET (Takamura and Nakajima 2004; Nakajima et al. 2007, 2020), another ground-based angular-scanning radiometer network, uses RSTAR in most of its analysis packages (Nakajima et al. 1996; Hashimoto et al. 2012; Kudo et al. 2021).

RSTAR is part of the STAR (System for Transfer of Atmospheric Radiation) series, which was developed and distributed by the OpenCLASTR project (<http://157.82.240.167/~clastr/>) led by some of the authors of this study. In addition to the scalar RTM (RSTAR), the STAR series includes a vector RTM called PSTAR (STAR for Polarized radiance calculations; Ota et al. 2010) and the flux calculation code FSTAR (STAR for Flux calculations; Nakajima et al. 2000), making it a broadly compatible group of packages. In particular, RSTAR and PSTAR introduce efficient calculation methods for IMS (Improved Multiple and Single scattering approximation; Nakajima and Tanaka 1988) and Pⁿ-IMS (IMS by *n*th order multiple scattering correction of the forward Peak; Momoi et al. 2022), respectively, enabling accurate reconstruction of sky radiances even in the solar aureole region. Therefore, these RTMs have been widely used in the analysis of satellite- and ground-based remote sensing observations,

especially by the Japanese research community (e.g., Takenaka et al. 2011; Hashimoto and Nakajima 2017; Sekiguchi et al. 2018; Shi et al. 2019). The STAR series efficiently computes multi-species gas-absorbing broadband radiative flux using the method of Sekiguchi and Nakajima (2008), which is a nonlinearly optimized version of the correlated *k*-distribution (CKD) method (Lacis and Oinas 1991; Fu and Liou 1992). For narrow-band gas absorption calculation, RSTAR uses the CKD method for which the standard LUT (hereafter, SN-CKD) was designed mechanically with two Gaussian quadrature points, as described in Sect. 2.2. Based on RSTAR with the SN-CKD, Momoi et al. (2020) proposed an approach using the SKYMAP algorithm, which retrieves the concentrations of atmospheric gases, such as water vapor, from the dependence of the angular distribution of diffuse radiance with a multi-term least squares method and calibrates the radiometric sensor using retrieved values, as described in Sect. 3.4.

Despite the progress described above, detailed assessment of the information contents of the water vapor and aerosols included in the direct solar irradiance and diffuse radiance is insufficient due to the large computational burden. The main instrument of the SKYNET is an angular-scanning radiometer called sky-radiometer (Prede, Tokyo, Japan) that measures direct solar and diffuses irradiances with a finite field of view at multiple wavelengths, including a water vapor absorption band (940 nm). From these measurements, we retrieve aerosol properties (e.g., size distribution, refractive index, and particle shape), cloud properties (e.g., effective radius and cloud optical thickness; Khatri et al. 2019), and ozone and water vapor amounts (Khatri et al. 2014; Uchiyama et al. 2014). In general, the column total atmospheric water vapor (precipitable water vapor [PWV]) is estimated from atmospheric transmittance in water vapor absorption regions, such as 940 nm, using observations taken with a photometer (Fowle 1912, 1915; Bruegge et al. 1992; Schmid et al. 1996, 2001; Halthore et al. 1997; Holben et al. 1998; Campanelli et al. 2014, 2018; Uchiyama et al. 2014, 2019). Campanelli et al. (2014, 2018) and Uchiyama et al. (2014, 2019) used the empirical equation: $\ln \tilde{T}_{\text{H}_2\text{O}} = -a(mw)^b$ (Bruegge et al. 1992) to define the relationship between the convolved transmittance of atmospheric water vapor ($\tilde{T}_{\text{H}_2\text{O}}$) and PWV (*w*). In this equation, *a* and *b* are adjustment parameters, which are affected by the filter response function of the radiometer and can be determined using several approaches, including comparison with other instruments (Campanelli et al. 2014, 2018) and theoretical calculations (Uchiyama et al. 2014; Giles et al. 2019). For determining the parameters through theoretical calculations, the AERONET (Giles et al. 2019) uses the line-by-line (LBL) method under a US standard atmosphere,

while Uchiyama et al. (2014) used the CKD method under Air Force Geophysics Laboratory (AFGL) standard atmospheres. However, Campanelli et al. (2014, 2018) reported that the parameters vary seasonally and spatially due to differences in the vertical profiles of water vapor, temperature, and pressure. Therefore, the parameters should be estimated seasonally and spatially, but implementation of this approach using the LBL method has a high computational cost. Obtaining the convolved transmittance requires regular sensor calibration, in which the sensor output of the extraterrestrial solar irradiance (or calibration constant) is determined at a specific site (e.g., Mauna Loa Observatory), as the convolved transmittance is the ratio of the sensor output of direct solar irradiance to the calibration constant. Recently, Momoi et al. (2020) reported that the angular distribution of diffuse radiances for the water vapor absorption band in the almucantar plane is affected by PWV and proposed another PWV retrieval method based on this relationship. This method is suitable for us with long-term observations because a calibration constant can be determined from the PWV data derived from the on-site angular distribution of diffuse radiance using the SKYMAP algorithm. This approach requires accurate computations of sky radiances in the water vapor absorption band by the RTM. Furthermore, new algorithms for simultaneous retrieval of water vapor and aerosols and assessment of the retrieval using the water vapor absorption band are needed, as the diffuse radiances at 940 nm in parts of the sky other than the almucantar plane contain information about aerosol vertical inhomogeneity (Momoi et al. 2020).

In this study, we developed LUTs for the CKD method in the 940 nm water vapor absorption region (WV-CKD), installed the WV-CKD in RSTAR to enable rapid and accurate computation of the 940 nm band for retrieval of PWV, and assessed the impact of the introduction of the LUTs on PWV estimations from the angular distribution of diffuse radiances, using actual ground-based angular-scanning radiometer observations in the water vapor absorption band. The WV-CKD was constructed through optimization of the quadrature values (point and weight) and numbers. Section 2 describes the methods and experimental setup used to create the WV-CKD, and Sect. 3 provides the results of simulations used to estimate the accuracy of the WV-CKD and its impact on PWV estimation from actual SKYNET sky-radiometer observations.

2 Methods/experimental design

Section 2.1 describes the RTM calculation accuracy required to analyze sky-radiometer observations. Section 2.2 examines the challenges facing the currently used LUT of the k distribution (SN-CKD) in RSTAR version 7 (RSTAR7) for narrow-band sky radiance computation around the 940 nm region. Section 2.3 describes the method used to create a new LUT of the k distribution.

2.1 RTM calculation accuracy requirements

The sky-radiometer measures direct solar and diffuse irradiances. In previous studies (e.g., Uchiyama et al. 2014; Momoi et al. 2020; Kudo et al. 2021), PWV was estimated from direct solar irradiance and/or “normalized radiance,” which is defined as the ratio of diffuse radiance to direct solar irradiance (Nakajima et al. 1996). Section 2.1.1 describes these values measured by the sky-radiometer. Section 2.1.2 describes the uncertainty of sky-radiometer observations.

2.1.1 Measurement of sky irradiance

The POM-01 sky-radiometer measures direct solar and diffuse irradiances with a finite field of view at seven wavelengths: 315, 400, 500, 675, 870, 940, and 1020 nm. The latest model, POM-02, measures irradiance at 340, 380, 1627, and 2200 nm in addition to those wavelengths. Diffuse irradiance is measured at scattering angles of 2, 3, 4, 5, 7, 10, 15, 20, 25, 30, 40, 50, 60, 70, 80, 90, 100, 110, 120, 130, 140, 150, and 160° in the almucantar and principal planes.

Assuming a narrow spectral band filter response function, direct solar and diffuse irradiances can be described by a radiative transfer equation in a plane-parallel non-refractive atmosphere as follows:

$$F_{ds}(\lambda) = \frac{F_0(\lambda)}{d^2} T(\lambda), \tag{1a}$$

$$F_{df}(\Theta, \lambda) = \frac{F_0(\lambda)\Delta\Omega}{|\mu|d^2} L(\Theta, \lambda), \tag{1b}$$

$$F_0(\lambda) \propto F_{sol}(\lambda), \tag{1c}$$

$$T(\lambda) \equiv \exp\left(-\frac{\tau(\lambda)}{|\mu_0|}\right), \tag{2a}$$

$$L(\Theta, \lambda) \equiv T(\lambda) \left\{ \int_0^{\tau(\lambda)} \exp\left[(\tau - t) \left(\frac{1}{|\mu_0|} - \frac{1}{|\mu|}\right)\right] \omega'(\lambda, t) P'(\Theta, \lambda, t) dt + q(\Theta, \lambda) \right\}, \tag{2b}$$

$$R(\Theta, \lambda) \equiv \frac{|\mu|F_{df}(\Theta; \lambda)}{F_{ds}(\lambda)\Delta\Omega} = \frac{L(\Theta, \lambda)}{T(\lambda)}, \quad (2c)$$

where F_{ds} is the sensor output current of the direct solar irradiance; F_{df} is the sensor output current of diffuse irradiance detected with a finite field of view ($\Delta\Omega$); F_0 is the calibration constant, which is the sensor output current for extraterrestrial solar irradiance (F_{sol}) at the mean distance between earth and the sun; T is transmittance; L is diffuse intensity defined as Eqs. (1b) and (2b); R is normalized radiance; d is the distance between Earth and the sun (AU); λ is wavelength; τ is total optical thickness; m_0 is the optical air mass, represented as $m_0 = 1/|\cos\theta_0| = 1/|\mu_0|$; $P'(\Theta, \lambda, \tau')$ and $o'(\lambda, \tau')$ are the total phase function and total single scattering albedo, respectively, at an altitude of $\tau = \tau'$; and q is the multiple scattering contribution. Although determination of T requires F_0 , R does not require F_0 due to the normalization. Hereafter, T and L are referred to as sky intensities. Assuming a single homogeneous layer, L can be simplified as follows:

$$L(\Theta, \lambda) = \omega\tau P(\Theta, \lambda)E(\mu, \lambda) + q(\Theta, \lambda)T(\lambda), \quad (3a)$$

$$E(\mu, \lambda) \equiv \begin{cases} T(\lambda) & \mu = \mu_0 \\ \left[\left(\frac{1}{|\mu_0|} - \frac{1}{|\mu|} \right) \tau(\lambda) \right]^{-1} \left[\exp\left(-\frac{\tau(\lambda)}{|\mu|}\right) - \exp\left(-\frac{\tau(\lambda)}{|\mu_0|}\right) \right] & \mu \neq \mu_0 \end{cases} \quad (3b)$$

Furthermore, assuming a wideband filter response function (ϕ), convolved F_{ds} and F_{df} (\tilde{F}_{ds} and \tilde{F}_{df}) with ϕ can be obtained through convolution of Eq. (1), as follows:

$$\tilde{F}_{ds}(\lambda) = \int \phi(\lambda)F_{ds}(\lambda)d\lambda = \frac{1}{d^2} \int \phi(\lambda)F_0(\lambda)T(\lambda)d\lambda, \quad (4a)$$

$$\tilde{F}_{df}(\lambda) = \int \phi(\lambda)F_{df}(\lambda)d\lambda = \frac{\Delta\Omega}{|\mu|d^2} \int \phi(\lambda)F_0(\lambda)L(\Theta, \lambda)d\lambda, \quad (4b)$$

$$\tilde{F}_0(\lambda) = \int \phi(\lambda)F_0(\lambda)d\lambda \propto \int \phi(\lambda)F_{sol}(\lambda)d\lambda. \quad (4c)$$

Hence, the convolved sky intensities (\tilde{T} and \tilde{L}) and convolved normalized radiance (\tilde{R}) are defined as follows:

$$\tilde{T}(\lambda) = \frac{\tilde{F}_{ds}(\lambda)d^2}{\tilde{F}_0(\lambda)} = \frac{\int \phi(\lambda)F_{sol}(\lambda)T(\lambda)d\lambda}{\int \phi(\lambda)F_{sol}(\lambda)d\lambda}, \quad (5a)$$

$$\tilde{L}(\Theta, \lambda) = \frac{\int \phi(\lambda)F_{sol}(\lambda)L(\Theta, \lambda)d\lambda}{\int \phi(\lambda)F_{sol}(\lambda)d\lambda}. \quad (5b)$$

$$\tilde{R}(\Theta, \lambda) \equiv \frac{\tilde{L}(\Theta, \lambda)}{\tilde{T}(\lambda)} = \frac{\int \phi(\lambda)F_{sol}(\lambda)L(\Theta, \lambda)d\lambda}{\int \phi(\lambda)F_{sol}(\lambda)T(\lambda)d\lambda}, \quad (5c)$$

Although sky radiance in weak gas absorption regions, such as at 340, 380, 400, 500, 675, 870, and 1020 nm in sky-radiometer observations, can be assumed to represent narrow spectral bands (Eq. [2]), sky radiance in gas absorption regions, such as the 940 nm band in sky-radiometer observations, requires convolution (Eq. [5]).

2.1.2 Uncertainty of sky-radiometer observations

In the SKYNET analysis algorithms (e.g., Momoi et al. 2020; Kudo et al. 2021) used with sky-radiometer observations, the measurement values are treated as $\ln\tilde{T}$ and $\ln\tilde{R}$, obtained using Eq. (5). The weighted values ($\sigma_{\tilde{T}}^2$ and $\sigma_{\tilde{R}}^2$) of the covariance matrix in the algorithms are expressed under the assumption that \tilde{F}_{ds} , \tilde{F}_{df} , and \tilde{F}_0 are independent of each other, as follows:

$$\sigma_{\tilde{T}}^2 = \sigma_{\tilde{F}_{ds}}^2 + \sigma_{\tilde{F}_0}^2, \quad (6a)$$

$$\sigma_{\tilde{R}}^2 = \sigma_{\tilde{F}_{df}}^2 + \sigma_{\tilde{F}_{ds}}^2, \quad (6b)$$

where $\sigma_{\tilde{F}_0}$ is the standard deviation of the sky-radiometer calibration constant ($\ln\tilde{F}_0$) or the relative error of \tilde{F}_0 , as

$\partial\ln\tilde{F}_0 \sim \frac{\partial\tilde{F}_0}{\tilde{F}_0}$, $\sigma_{\tilde{F}_{ds}}$ and $\sigma_{\tilde{F}_{df}}$ are the standard deviations of sky-radiometer measurements ($\ln\tilde{F}_{ds}$ and $\ln\tilde{F}_{df}$, respectively).

In this study, we estimated $\sigma_{\tilde{F}_{ds}}$ from 10×10 radiances sampled at 0.1° intervals in a circumsolar domain of $\pm 1^\circ$ in both the zenith and azimuth angle directions. This measurement protocol is mainly used for calibration of the solid view angle through the solar disk scan method (Nakajima et al. 1996, 2020; Boi et al. 1999; Uchiyama et al. 2018). The solar disk scan method provides a solar aureole angular distribution (Fig. 1), which reduces observational noise with a Gaussian filter. Therefore, the uncertainty of sky intensity data is calculated from the difference (Δ_f) of sky irradiance between observed and Gaussian-filtered data, as follows:

$$\Delta_f = \ln f^{\text{obs}}(\Theta) - \ln f^{\text{gf}}(\Theta), \quad (7)$$

where f^{obs} and f^{gf} are the observed and Gaussian-filtered sky irradiances, respectively. Because the magnitude of the solar aureole angular distribution differs at large scattering angles ($\Theta \geq 0.3^\circ$), we used a range of 0.3° . Therefore, we could estimate the uncertainties of \tilde{F}_{ds} from Δ_f , as the solar disk diameter is approximately 0.5° . Figure 2 shows an example histogram of Δ_f at 340, 500,

and 940 nm based on measurements taken with the sky-radiometer POM-02 (serial no. PS2501401) on February 27 and 28, 2020, in Akiruno, Tokyo (35.751°N, 139.323°E). Table 1 lists the uncertainties of \bar{F}_{ds} and indicates that the standard deviation of sky-radiometer measurements ($\sigma_{\bar{F}_{ds}}$) at all wavelengths is less than 5.0×10^{-3} . Thus, $\sigma_{\bar{F}_{df}}$ is expected to be larger than $\sigma_{\bar{F}_{ds}}$. This is because \bar{F}_{ds} and \bar{F}_{df} are measured using the same detector, but $\bar{F}_{ds} \gg \bar{F}_{df}$ by the solar incident beam. Therefore, 5.0×10^{-3} is a reasonable benchmark value for errors in \bar{F}_{ds} and \bar{F}_{df} in this study.

2.2 Challenges regarding the *k*-distribution lookup table in RSTAR

In RSTAR7, gas absorption is considered for H₂O, CO₂, O₃, N₂O, CO, CH₄, and O₂ using HITRAN 2004 database (Rothman et al. 2005) and MT_CKD version 1 (Mlawer et al. 2012) for continuum absorptions. Gas absorption is calculated using the CKD method with a LUT (ckd.g.ch_2_2e3; SN-CKD), which generates two Gaussian quadrature points without optimization in each sub-band. The resolution of the SN-CKD at wavenumber (*k*) is $d\log_{10}k = 5 \times 10^{-4}$ ($dk \approx 12.2\text{cm}^{-1}$ at 940 nm). In weak gas absorption regions (e.g., sky-radiometer measurements at 340, 380, 400, 500, 675, 870, and 1020 nm), the radiance can be accurately computed using the SN-CKD because the gas absorption coefficient is small relative to other processes (e.g., Rayleigh scattering and aerosol extinction). However, careful consideration of the quadrature numbers is essential in the water vapor absorption region around 940 nm due to the complex absorption characteristics of water vapor. Therefore, we validated the radiance calculation with SN-CKD around 940 nm (10,000–10,900 cm⁻¹ [1000–917 nm]) through

the LBL method using simulated band-averaged sky intensities for sub-bands ($\bar{T} = \frac{\bar{F}_{ds}}{\bar{F}_0}$ and $\bar{L} = \frac{|\mu| \bar{F}_{df}(\Theta, \lambda)}{\bar{F}_0(\lambda) \Delta\Omega}$). The LBL method is based on the line absorption calculation from HITRAN 2012 (Rothman et al. 2013) and continuum absorption from MT_CKD version 3.2 (Mlawer et al. 2012). The band-averaged sky intensities for sub-bands were computed using RSTAR7 with the IMS method (Nakajima and Tanaka 1988). The validation dataset (CA-DB) consisted of band-averaged sky intensities at ground level, which were calculated from continental averaged aerosol conditions (Hess et al. 1999) with aerosol optical thickness (AOT) of 0.05, 0.20, and 1.00 at 940 nm; solar zenith angles of 30, 50, and 70 degrees in two sky-radiometer observation planes (almucantar and principal); and PWV from 0.5 to 6 cm at an interval of 0.5 cm. The vertical atmospheric profile is the US standard atmosphere employed in RSTAR7. Extraterrestrial

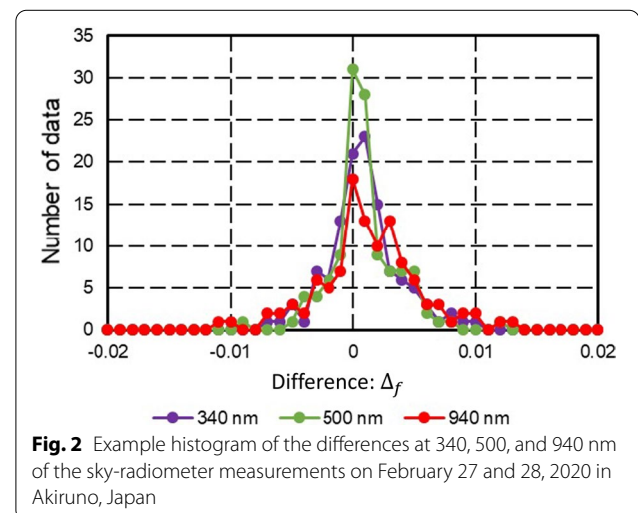


Fig. 2 Example histogram of the differences at 340, 500, and 940 nm of the sky-radiometer measurements on February 27 and 28, 2020 in Akiruno, Japan

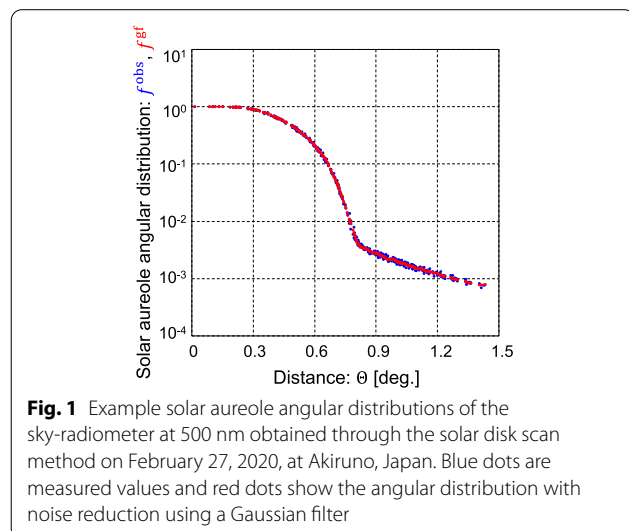


Fig. 1 Example solar aureole angular distributions of the sky-radiometer at 500 nm obtained through the solar disk scan method on February 27, 2020, at Akiruno, Japan. Blue dots are measured values and red dots show the angular distribution with noise reduction using a Gaussian filter

Table 1 Uncertainty of sky irradiance based on comparison between f^{obs} and f^{gf}

Wavelength	Num. of data	Standard deviation
315 nm	127	5.0×10^{-3}
340 nm	117	3.0×10^{-3}
380 nm	104	1.9×10^{-3}
400 nm	122	2.7×10^{-3}
500 nm	119	2.9×10^{-3}
675 nm	114	4.1×10^{-3}
870 nm	135	6.5×10^{-3}
1020 nm	105	4.3×10^{-3}
940 nm	110	4.3×10^{-3}
1627 nm	56	4.8×10^{-3}
2200 nm	57	4.4×10^{-3}

solar irradiance was averaged at the sub-band ($\text{dlog}_{10}k$) level. Therefore, with the LBL method, \bar{T} and \bar{L} are expressed as:

$$\varepsilon_{\bar{L},RT}^2(\bar{\lambda}; \Theta, \theta_0, w, \tau_a) = \left(\ln \frac{\bar{L}^{\text{LBL}}}{\bar{L}^{\text{CKD}}} \right)^2, \quad (10b)$$

$$\varepsilon_{\bar{T},\text{max}}^2(\bar{\lambda}) = \max \left\{ \varepsilon_{\bar{T},RT}^2(\bar{\lambda}), \varepsilon_{\bar{L},RT}^2(\bar{\lambda}) \mid \theta_0 = 30(20)70^\circ; w = 0.5(0.5)6\text{cm}; \tau_a = 0.05, 0.2, 1.0 \right\}. \quad (10c)$$

$$\bar{T}^{\text{LBL}}(\bar{\lambda}) = \frac{1}{\int_{\Delta_k} \frac{dk}{k^2}} \int_{\Delta_k} T_A(\lambda) T_R(\lambda) T_{\text{H}_2\text{O}}(\lambda) T_{\text{cont}}(\lambda) \frac{dk}{k^2}, \quad (8a)$$

$$\bar{L}^{\text{LBL}}(\Theta, \bar{\lambda}) = \frac{1}{\int_{\Delta_k} \frac{dk}{k^2}} \int_{\Delta_k} T_A(\lambda) T_R(\lambda) T_{\text{H}_2\text{O}}(\lambda) T_{\text{cont}}(\lambda) R(\Theta, \lambda) \frac{dk}{k^2}, \quad (8b)$$

where T_A and T_R are the monochromatic transmittances of aerosol extinction and Rayleigh scattering, respectively; $T_{\text{H}_2\text{O}}$ is the monochromatic transmittance of water vapor absorption (line and self-continuum); and T_{cont} is the monochromatic transmittance of the O_2 and O_3 continuum absorption. Because the differential interval of the numerical integral is too small ($dk = 0.01\text{cm}^{-1}$) for use with the LBL method, $T_{\text{H}_2\text{O}}$ is obtained using Beer-Lambert's law as follows:

$$\ln[T_{\text{H}_2\text{O}}(\lambda)] = -m_0(\theta_0) \int_0^z [\sigma_{\text{H}_2\text{O},\text{line}}(K, p, \lambda) + \sigma_{\text{H}_2\text{O},\text{cont}}(K, \lambda)] dz, \quad (9)$$

where $\sigma_{\text{H}_2\text{O},\text{line}}$ and $\sigma_{\text{H}_2\text{O},\text{cont}}$ are the absorption coefficients [m^{-1}] of the water vapor line and self-continuum absorptions, respectively; K is the temperature; p is the pressure; and z is the geometric thickness of the atmosphere [m]. Figure 3 shows the maximum errors ($\varepsilon_{\bar{T},\text{max}}$) of \bar{T} and \bar{L} obtained with the SN-CKD compared with the LBL method, which were determined as:

$$\varepsilon_{\bar{T},RT}^2(\bar{\lambda}; \theta_0, w, \tau_a) = \left(\ln \frac{\bar{T}^{\text{LBL}}}{\bar{T}^{\text{CKD}}} \right)^2, \quad (10a)$$

The root mean square errors of $\varepsilon_{\bar{T},\text{max}}$ for CA-DB were 8.24×10^{-1} (approximately 82.4% error) at $10,000\text{--}10,902 \text{ cm}^{-1}$, and 1.16 (approximately 116% error) at $10,411\text{--}10,864 \text{ cm}^{-1}$ [961–920 nm]. This error propagates to the convolved sky intensities. Thus, the error of convolved sky intensities with a filter response function of Gaussian shape at a full width at half maximum (FWHM) of 10 nm, corresponding to the FWHM of the sky-radiometer's filter, reaches 22%, as discussed in Sect. 3.2. This residual error is larger than $\sigma_{F,\text{ds}}$. One reason for this large error is an update of the absorption database from HITRAN 2004 to HITRAN 2012 where the number of water vapor absorption lines in this band increased more than fourfold. Another reason is the lack of optimization, which leads large error under the US atmosphere.

2.3 Method used to create the new k -distribution lookup table

In this study, a new LUT of the k distribution at 10-cm^{-1} intervals (Δ_k) from $10,000 \text{ cm}^{-1}$ to $10,900 \text{ cm}^{-1}$ (hereafter WV-CKD-10) was constructed through optimization of the quadrature values (point and weight) and numbers through the LBL method. Radiation around 940 nm is attenuated mainly through aerosol extinction, Rayleigh scattering, and gas absorption including O_2 continuum, O_3 continuum, and water vapor line and self-continuum absorptions. Thus, WV-CKD-10 consists of three LUTs: quadrature weights, water vapor k distribution, and O_2 and O_3 continuums. Those LUTs were created from

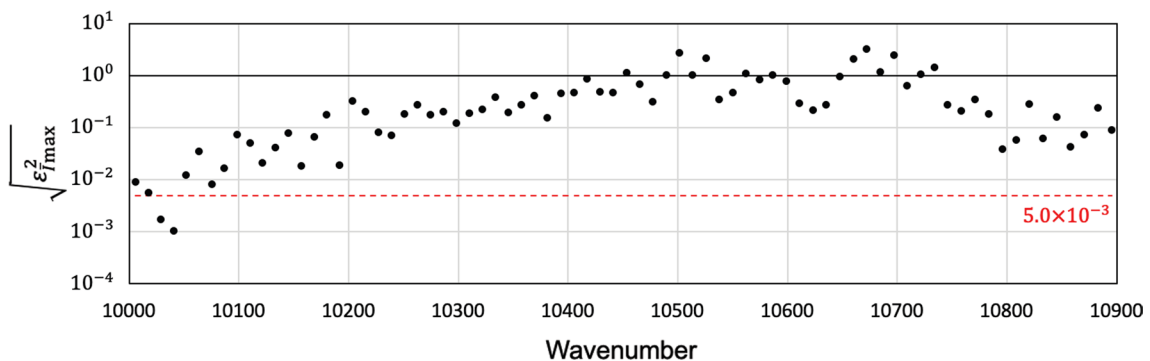


Fig. 3 The maximum error of the SN-CKD with CA-DB. SN-CKD is the standard lookup table for the CKD method in the radiative transfer model RSTAR. CA-DB is dataset consisting of radiances at ground level under continental averaged aerosol condition of Hess et al. (1999)

HITRAN 2012 (Rothman et al. 2013) and MT_CKD version 3.2 (Mlawer et al. 2012). Because computation of the RTM requires the number of quadrature values, WV-CKD optimally contains the minimum quadrature numbers in addition to quadrature values optimized for $\bar{E}(\mu, \lambda)$ under six AFGL standard atmospheres (US standard, tropical, mid-latitude summer, mid-latitude winter, high-latitude summer, and high-latitude winter) in RSTAR7. In this study, the maximum error ($\sqrt{\varepsilon_E^2}$) of $\bar{E}(\mu, \lambda)$ for $\Delta_\kappa = 10\text{cm}^{-1}$ is achieved at values less than 5.0×10^{-3} . The quadrature values, consisting of a pair of point and weight values, were optimized with the Gauss–Newton method, and the quadrature numbers were determined through a linear search from 2 to 64. After construction of the WV-CKD-10, we validated it with CA-DB, as described in the previous subsection for the validation dataset of the SN-CKD.

3 Results and discussion

3.1 Optimized k -distribution lookup table

Figure 4a shows the quadrature numbers and Fig. 4b shows the maximum error ($\sqrt{\varepsilon_{T_{\text{max}}}^2}$), which was satisfied at values less than 5.0×10^{-3} for 10,000–10,900 cm^{-1} . The quadrature number falls into the range of 3–15 at 10,000–10,900 cm^{-1} and 4–15 at 10,410–10,870 cm^{-1} [961–920 nm]. The median quadrature number is 7 at 10,000–10,900 cm^{-1} and 8 at 10,410–10,870 cm^{-1} [961–920 nm], as the water vapor line absorption around 940 nm is complex and requires numerous quadrature points to maintain accuracy. In conclusion, using the WV-CKD-10 reduces the number of executions of the RTM to approximately 1/100 of the number needed for the LBL method, as the band-averaged sky intensities at 10 cm^{-1} must be computed 1000 times with the LBL method ($= 10\text{cm}^{-1}/0.01\text{cm}^{-1}$) in RSTAR7 (Table 2).

The equations for band-averaged sky intensities differ markedly between the LBL and CKD methods. \bar{T}^{CKD} and \bar{L}^{CKD} , derived using the WV-CKD, are as follows:

$$\bar{T}^{\text{CKD}}(\lambda) = \bar{T}_A(\lambda) \bar{T}_R(\lambda) \bar{T}_{\text{cont}}(\lambda) \sum_{i=1}^{N_{\text{ch}}} \xi_i T_{\text{H}_2\text{O,ckd}}^{(i)}(\lambda), \quad (11a)$$

$$\begin{aligned} \bar{L}^{\text{CKD}}(\Theta, \lambda) &= \bar{T}_A(\lambda) \bar{T}_R(\lambda) \bar{T}_{\text{cont}}(\lambda) \\ &\sum_{i=1}^{N_{\text{ch}}} \xi_i T_{\text{H}_2\text{O,ckd}}^{(i)}(\lambda) R^{(i)}(\Theta, \lambda), \end{aligned} \quad (11b)$$

where \bar{T}_A and \bar{T}_R are the band-averaged values of T_A and T_R , respectively; N_{ch} is the number of quadrature points; $T_{\text{H}_2\text{O,ckd}}^{(i)}$ and $R^{(i)}$ are the i th transmittance and normalized radiance of the quadrature values of the k distribution at Δ_κ , respectively; and ξ_i is the i th quadrature weight of the k distribution at Δ_κ , which is normalized to:

$$\sum_{i=1}^{N_{\text{ch}}} \xi_i = 1. \quad (12)$$

In the CKD method, convolved sky intensities (\hat{T} and \hat{L}) are determined with the stepwise filter response function $\bar{\phi}$, as follows:

$$\hat{T}(\lambda) = \frac{\sum^{N_s} \bar{\phi} \cdot \bar{F}_{\text{sol}} \cdot \bar{T} \cdot \Delta_\kappa \bar{\lambda}^2}{\sum^{N_s} \bar{\phi} \cdot \bar{F}_{\text{sol}} \cdot \Delta_\kappa \bar{\lambda}^2}, \quad (13a)$$

$$\hat{L}(\Theta, \lambda) = \frac{\sum^{N_s} \bar{\phi} \cdot \bar{F}_{\text{sol}} \cdot \bar{L} \cdot \Delta_\kappa \bar{\lambda}^2}{\sum^{N_s} \bar{\phi} \cdot \bar{F}_{\text{sol}} \cdot \Delta_\kappa \bar{\lambda}^2}. \quad (13b)$$

$$\bar{F}_{\text{sol}}(\bar{\lambda}) \equiv \frac{\int_{\Delta_\kappa} F_{\text{sol}}(\lambda) \frac{d\lambda}{\kappa^2}}{\Delta_\kappa \bar{\lambda}^2}, \quad (13c)$$

$$\bar{\phi}(\bar{\lambda}) \equiv \frac{\int_{\Delta_\kappa} \phi(\lambda) \frac{d\lambda}{\kappa^2}}{\Delta_\kappa \bar{\lambda}^2}, \quad (13d)$$

where \bar{F}_{sol} is the band-averaged extraterrestrial solar irradiance and N_s is the number of sub-bands. \hat{T} and \hat{L} in Eq. (5a) (\hat{L} and \bar{L} in Eq. (5b)) are not entirely synonymous, but are generally equivalent based on the assumption that the extraterrestrial solar irradiance and filter response function being nearly constant across sub-bands. The residual errors ($\varepsilon_{\hat{T},\text{RT}}$ and $\varepsilon_{\hat{L},\text{RT}}$) of \hat{T} and \hat{L} for the CKD method are obtained as follows:

$$\begin{aligned} \varepsilon_{\hat{T},\text{RT}}^2 &= \left(\ln \frac{\sum^{N_s} \bar{\phi} \cdot \bar{F}_{\text{sol}} \cdot \bar{T}^{\text{CKD}} \cdot \Delta_\kappa \bar{\lambda}^2}{\sum^{N_s} \bar{\phi} \cdot \bar{F}_{\text{sol}} \cdot \bar{T}^{\text{LBL}} \cdot \Delta_\kappa \bar{\lambda}^2} \right)^2 \\ &\sim \left[\frac{(\sum^{N_s} \bar{\phi} \cdot \bar{F}_{\text{sol}} \cdot \bar{T}^{\text{CKD}} \cdot \Delta_\kappa \bar{\lambda}^2) - (\sum^{N_s} \bar{\phi} \cdot \bar{F}_{\text{sol}} \cdot \bar{T}^{\text{LBL}} \cdot \Delta_\kappa \bar{\lambda}^2)}{\sum^{N_s} \bar{\phi} \cdot \bar{F}_{\text{sol}} \cdot \bar{T}^{\text{LBL}} \cdot \Delta_\kappa \bar{\lambda}^2} \right]^2 \\ &= \frac{\sum^{N_s} [\bar{\phi} \cdot \bar{F}_{\text{sol}} \cdot \bar{T}^{\text{LBL}} \cdot \varepsilon_{\hat{T},\text{RT}} \cdot \Delta_\kappa \bar{\lambda}^2]^2}{[\sum^{N_s} \bar{\phi} \cdot \bar{F}_{\text{sol}} \cdot \bar{T}^{\text{LBL}} \cdot \Delta_\kappa \bar{\lambda}^2]^2}, \end{aligned} \quad (14a)$$

$$\begin{aligned} \varepsilon_{\hat{L},\text{RT}}^2(\Theta) &= \left(\ln \frac{\sum^{N_s} \bar{\phi} \cdot \bar{F}_{\text{sol}} \cdot \bar{L}^{\text{CKD}}(\Theta) \cdot \Delta_\kappa \bar{\lambda}^2}{\sum^{N_s} \bar{\phi} \cdot \bar{F}_{\text{sol}} \cdot \bar{L}^{\text{LBL}}(\Theta) \cdot \Delta_\kappa \bar{\lambda}^2} \right)^2 \\ &\sim \left[\frac{(\sum^{N_s} \bar{\phi} \cdot \bar{F}_{\text{sol}} \cdot \bar{L}^{\text{CKD}}(\Theta) \cdot \Delta_\kappa \bar{\lambda}^2) - (\sum^{N_s} \bar{\phi} \cdot \bar{F}_{\text{sol}} \cdot \bar{L}^{\text{LBL}}(\Theta) \cdot \Delta_\kappa \bar{\lambda}^2)}{\sum^{N_s} \bar{\phi} \cdot \bar{F}_{\text{sol}} \cdot \bar{L}^{\text{LBL}}(\Theta) \cdot \Delta_\kappa \bar{\lambda}^2} \right]^2 \\ &= \frac{\sum^{N_s} [\bar{\phi} \cdot \bar{F}_{\text{sol}} \cdot \bar{L}^{\text{LBL}}(\Theta) \cdot \varepsilon_{\hat{L},\text{RT}} \cdot \Delta_\kappa \bar{\lambda}^2]^2}{[\sum^{N_s} \bar{\phi} \cdot \bar{F}_{\text{sol}} \cdot \bar{L}^{\text{LBL}}(\Theta) \cdot \Delta_\kappa \bar{\lambda}^2]^2}, \end{aligned} \quad (14b)$$

$$\varepsilon_{T_{\text{max}}}^2 = \max \left\{ \varepsilon_{\hat{T},\text{RT}}^2, \varepsilon_{\hat{L},\text{RT}}^2(\Theta) \right\}. \quad (14c)$$

If we assume that $\bar{T}_{\text{H}_2\text{O}}$ is roughly randomly distributed in the range of $\bar{T}_{\text{H}_2\text{O},\text{min}} = 0$ to $\bar{T}_{\text{H}_2\text{O},\text{max}} = 1$, $\varepsilon_{\hat{T},\text{RT}}^2$ and $\varepsilon_{\hat{L},\text{RT}}^2$ are obtained as follows:

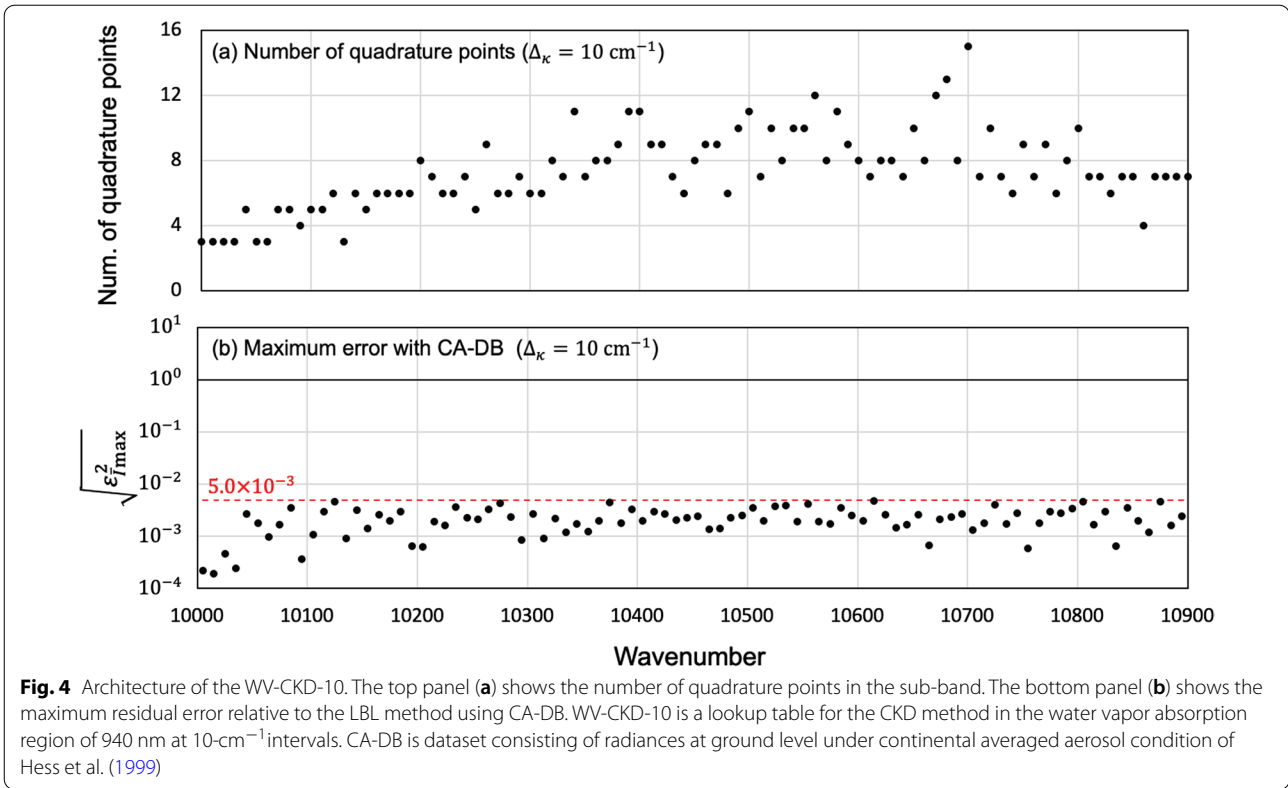


Table 2 Description of the WV-CKDs. WV-CKD is a series of lookup tables for the CKD method in the water vapor absorption region of 940 nm at 2-, 5-, and 10-cm⁻¹ intervals

	WV-CKD-2	WV-CKD-5	WV-CKD-10	LBL
Resolution	2 cm ⁻¹	5 cm ⁻¹	10 cm ⁻¹	0.01 cm ⁻¹
Maximum error of $E(\mu, \lambda): (\varepsilon_{\bar{E}}^2)^{1/2}$	11.2×10^{-3}	7.1×10^{-3}	5.0×10^{-3}	-
Median quadrature numbers (10,000–10,900 cm ⁻¹)	4	6	7	-
Median quadrature numbers (10,410–10,870 cm ⁻¹)	5	6	8	-
Mean computation times (10,000–10,900 cm ⁻¹)	2.18/cm ⁻¹	1.18/cm ⁻¹	0.734/cm ⁻¹	100/cm ⁻¹
Mean computation times (10,410–10,870 cm ⁻¹)	2.44/cm ⁻¹	1.33/cm ⁻¹	0.848/cm ⁻¹	100/cm ⁻¹
$D\Phi$ of Eq. 16 (FWHM = 5 nm)	0.176	0.280	0.394	-
$D\Phi$ of Eq. 16 (FWHM = 10 nm)	0.124	0.198	0.278	-
$D\Phi$ of Eq. 16 (FWHM = 15 nm)	0.102	0.162	0.228	-

$$\varepsilon_{\bar{T},RT}^2 \sim \varepsilon_{\bar{L},RT}^2 \sim D^2 \Phi^2 < \varepsilon_{I_{\max}}^2 >, \tag{15}$$

where $\langle \rangle$ indicates an averaging operation;

$$D^2 \equiv \frac{\langle (\bar{T}^{LBL})^2 \rangle}{\langle \bar{T}^{LBL} \rangle^2} \sim \frac{\int_{\bar{T}_{H2O,\min}}^{\bar{T}_{H2O,\max}} x^2 dx}{\bar{T}_{H2O,\max} - \bar{T}_{H2O,\min}} \tag{16a}$$

$$/ \left(\frac{\int_{\bar{T}_{H2O,\min}}^{\bar{T}_{H2O,\max}} x dx}{\bar{T}_{H2O,\max} - \bar{T}_{H2O,\min}} \right)^2 = \frac{4}{3} \approx 1.33,$$

$$\Phi^2 \equiv \frac{\sum^{N_s} [\bar{\phi} \cdot \bar{F}_{sol} \cdot \Delta_{\kappa} \bar{\lambda}^{-2}]^2}{\left[\sum^{N_s} \bar{\phi} \cdot \bar{F}_{sol} \cdot \Delta_{\kappa} \bar{\lambda}^{-2} \right]^2} \sim (0.242)^2. \tag{16b}$$

In Eq. (15), $\varepsilon_{\bar{T},RT} \sim \varepsilon_{\bar{L},RT} \sim \langle \varepsilon_{I_{\max}}^2 \rangle$. The second term on the right-hand side of Eq. (16a) is a rough assumption because of the biased probability distribution of \bar{T}^{LBL} . For example, D^2 is 1.18, 1.38, and 1.82 at 10,410–10,870 cm⁻¹ [961–920 nm] under the US standard atmosphere with a respective PWV of 0.7, 1.4, and 2.8 cm and a

solar zenith angle of 70 degrees. The second expression on the right-hand side of Eq. (16b) is an estimate for the situation in which the FWHM is 10 nm and the central wavelength is 940 nm using the extraterrestrial solar irradiance reported by Coddington et al. (2021). Moreover, the residual error ($\varepsilon_{\hat{R},RT}$) of the convolved normalized radiance (\hat{R}) with the stepwise filter response function is obtained as follows:

$$\begin{aligned} \hat{R}^{\text{CKD}}(\Theta) &\equiv \frac{\hat{L}^{\text{CKD}}}{\hat{T}^{\text{CKD}}(\Theta)} \\ &= \hat{R}^{\text{LBL}}(\Theta)e^{\varepsilon_{\hat{R},RT}(\Theta)} \\ &= \hat{R}^{\text{LBL}}(\Theta)e^{\varepsilon_{\hat{L},RT}(\Theta) - \varepsilon_{\hat{T},RT}}, \end{aligned} \tag{17a}$$

$$\varepsilon_{\hat{R},\text{max}}^2 = \max\left\{\varepsilon_{\hat{R},RT}^2(\Theta)\right\}. \tag{17b}$$

Using Eqs. (10) and (15), $\varepsilon_{\hat{T},\text{max}}^2$ is estimated as $\varepsilon_{\hat{T},\text{max}}^2 \sim D^2\Phi^2 < \varepsilon_{\hat{L},\text{max}}^2 \sim (D\Phi\varepsilon_E)^2$ and the expected residual errors of radiances simulated with the WV-CKD are estimated as follows:

$$\begin{aligned} \varepsilon_{\hat{T},RT}^2 &\sim \varepsilon_{\hat{L},RT}^2 \leq \varepsilon_{\hat{L},\text{max}}^2 \\ &\sim (D\Phi\varepsilon_E)^2 \sim (0.278)^2 \\ &\times \left(5.0 \times 10^{-3}\right)^2 \ll \sigma_{F_{\text{ds}}}^2 \sim \sigma_{F_{\text{df}}}^2. \end{aligned} \tag{18}$$

3.2 Evaluation of the WV-CKD

To evaluate sky radiance at ground level in detail, we constructed a fine-scale LUT of the k distribution ($\Delta_k = 2,5\text{cm}^{-1}$; hereinafter, WV-CKD-2 and WV-CKD-5, respectively) in the manner described in Sec. 2.3; in this case, $\sqrt{\varepsilon_E^2}$ was satisfied at values below 11.2×10^{-3} and 7.1×10^{-3} to maintain accuracy of the 10cm^{-1} band-averaged sky intensities below 5.0×10^{-3} (equal to that of the WV-CKD-10). The details of the WV-CKD-2 and WV-CKD-5 are summarized in Table 2. The quadrature numbers of the WV-CKD-2 and WV-CKD-5 fall into the ranges of 1–9 and 2–11, respectively. The median quadrature numbers of the WV-CKD-2 and WV-CKD-5 are 4 and 6, respectively. Therefore, using all of the WV-CKD developed here allows for ≥ 46 -fold more rapid calculation than the LBL method. The simulation (using a dataset consisting of sky intensities at ground level under several aerosol conditions from Dubovik et al. 2000; hereinafter, DU-DB) was conducted for the two aerosol types reported by Dubovik et al. (2000) and two atmospheric profiles, described in Table 3. The atmospheric profiles used represented the SKYNET Chiba site (35.63°N, 140.10°E) and were obtained from National Centers for Environmental Prediction (NCEP) reanalysis

1 data for 2018 (Fig. 5). The sky intensities were convolved using filter response functions for three Gaussian shapes (FWHM: 5, 10, 15 nm) at two central wavelengths of 936 and 940 nm (Fig. 6).

3.2.1 Comparison with convolved sky intensities obtained using the stepwise filter response function

\hat{T}^{LBL} , \hat{L}^{LBL} , and \hat{R}^{LBL} assume that the extraterrestrial solar irradiance and filter response function are nearly constant in each sub-band. Therefore, this section aims to evaluate whether the WV-CKD can be used for aerosol and atmospheric vertical profiles other than the six AFGL standard atmospheres with continental averaged aerosols.

Table 4 summarizes the maximum residuals obtained between the LBL and CKD methods. The expected values ($D\Phi\sqrt{\varepsilon_E^2}$) estimated using Eq. (15) in each simulation are also presented in Table 4. The $\sqrt{\varepsilon_{\hat{T},\text{max}}^2}$ values obtained using all WV-CKD were smaller than 1.64×10^{-3} and similar to the expected residual errors ($D\Phi\sqrt{\varepsilon_E^2} = 2.0 \times 10^{-3}, 1.4 \times 10^{-3}$ and 1.1×10^{-3} at FWHM of 5, 10, and 15 nm, respectively). In some cases, the residual errors exceed $D\Phi\sqrt{\varepsilon_E^2}$, but fall within two standard deviations ($2D\Phi\sqrt{\varepsilon_E^2}$) due to fluctuations in transmittance [Eq. (16a)]. This suggests that the WV-CKD can be used under conditions other than the six AFGL standard atmospheres with continental averaged aerosols; moreover, the expected residual error ($D\Phi\sqrt{\varepsilon_E^2}$) is a useful benchmark of \hat{T}^{CKD} and \hat{L}^{CKD} . Additionally, the $\sqrt{\varepsilon_{\hat{R},\text{max}}^2}$ values were smaller than 3.97×10^{-4} and much smaller than $\sqrt{\varepsilon_{\hat{T},\text{max}}^2}$. This difference arises because the normalized radiance cancels the residual error of \hat{T}^{CKD} and \hat{L}^{CKD} , as shown in Eq. (17a). In contrast, the $\sqrt{\varepsilon_{\hat{T},\text{max}}^2}$ values obtained using the SN-CKD were much larger, ranging from 7.53×10^{-3} to 2.21×10^{-1} , and were not negligible relative to the uncertainty of sky-radiometer observations. Thus, the $\sqrt{\varepsilon_{\hat{R},\text{max}}^2}$ of the SN-CKD is better than $\sqrt{\varepsilon_{\hat{T},\text{max}}^2}$, but reaches 6.71×10^{-2} at the FWHM of 5 nm and 3.89×10^{-2} at an FWHM of 10 nm.

3.2.2 Comparison with convolved sky intensities obtained using a smooth filter response function

\tilde{T}^{LBL} , \tilde{L}^{LBL} , and \tilde{R}^{LBL} are calculated using the LBL method and convolved with a smooth filter response function and the high-resolution (0.01cm^{-1}) extraterrestrial solar irradiance data from Coddington et al. (2021). This section provides a comprehensive assessment of \hat{T}^{CKD} , \hat{L}^{CKD} , and \hat{R}^{CKD} in addition to the general performance of gas absorption discussed in Sect. 3.2.1. The residual errors of the convolved sky intensities are defined as follows:

Table 3 Description of the simulation data used in Sec 3.2 (DU-DB)

Element	Variable	Type 1	Type 2	Type 3	Type 4
Aerosol	Component (Dubovik et al. 2000)	Water-soluble		Biomass burning	
	Vertical profile	$\exp(-z/H), H=2$ km		$\exp(-z/H), H=4$ km	
	Optical depth at 500 nm	0.2		0.4	
Atmosphere	Vertical profile	Chiba Jan	Chiba-Apr	Chiba-Jul	Chiba-Oct
	PWV	0.78 cm	1.79 cm	4.64 cm	2.58 cm
Geometry	Solar zenith angle	60 degree		40 degree	

$$\varepsilon_T^2 = \left(\ln \frac{\widehat{T}^{CKD}}{\widetilde{T}^{LBL}} \right)^2 = \left[\ln \left(\frac{\sum N_s \bar{\phi} \cdot \bar{F}_{sol} \cdot \bar{T}^{CKD} \cdot \Delta_k \bar{\lambda}^2}{\sum N_s \bar{\phi} \cdot \bar{F}_{sol} \cdot \Delta_k \bar{\lambda}^2} / \frac{\int \phi(\lambda) F_{sol}(\lambda) T^{LBL}(\lambda) d\lambda}{\int \phi(\lambda) F_{sol}(\lambda) d\lambda} \right) \right]^2 \sim \varepsilon_{T,RT}^2 + \varepsilon_{T,FRF}^2, \quad (19a)$$

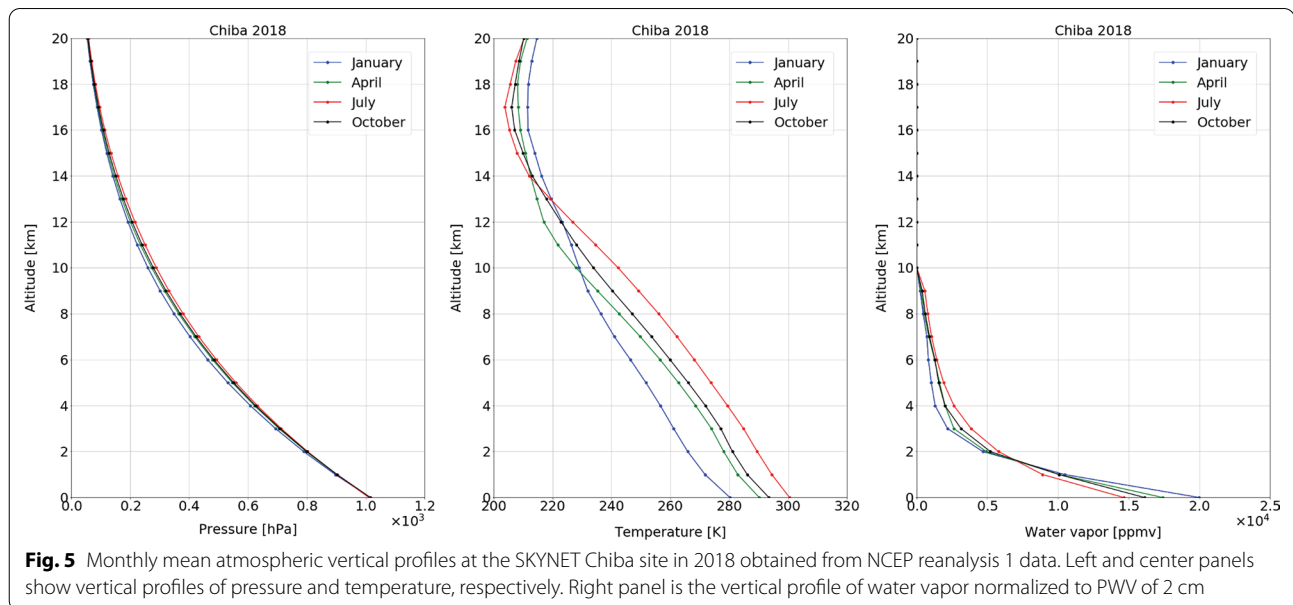
$$\varepsilon_L^2(\Theta) = \left(\ln \frac{\widehat{L}^{CKD}}{\widetilde{L}^{LBL}} \right)^2 = \left[\ln \left(\frac{\sum N_s \bar{\phi} \cdot \bar{F}_{sol} \cdot \bar{L}^{CKD}(\Theta) \cdot \Delta_k \bar{\lambda}^2}{\sum N_s \bar{\phi} \cdot \bar{F}_{sol} \cdot \Delta_k \bar{\lambda}^2} / \frac{\int \phi(\lambda) F_{sol}(\lambda) L^{LBL}(\Theta, \lambda) d\lambda}{\int \phi(\lambda) F_{sol}(\lambda) d\lambda} \right) \right]^2 \sim \varepsilon_{L,RT}^2 + \varepsilon_{L,FRF}^2, \quad (19b)$$

$$\varepsilon_R^2(\Theta) = \left[\ln \left(\frac{\widehat{L}^{CKD}}{\widetilde{T}^{CKD}} / \frac{\widetilde{L}^{LBL}}{\widetilde{T}^{LBL}} \right) \right]^2 = \left[\ln \left(\frac{\sum N_s \bar{\phi} \cdot \bar{F}_{sol} \cdot \bar{L}^{CKD}(\Theta) \cdot \Delta_k \bar{\lambda}^2}{\sum N_s \bar{\phi} \cdot \bar{F}_{sol} \cdot \bar{T}^{CKD} \cdot \Delta_k \bar{\lambda}^2} / \frac{\int \phi(\lambda) F_{sol}(\lambda) L^{LBL}(\Theta, \lambda) d\lambda}{\int \phi(\lambda) F_{sol}(\lambda) T^{LBL}(\lambda) d\lambda} \right) \right]^2, \quad (19c)$$

where $\varepsilon_{T,FRF}^2$ and $\varepsilon_{L,FRF}^2$ are the residual errors arising from the assumptions of the extraterrestrial solar irradiance and filter response function. The maximum residuals can be obtained as follows:

$$\varepsilon_{Tmax}^2 = \max \{ \varepsilon_T^2, \varepsilon_L^2(\Theta) \}, \quad (20a)$$

$$\varepsilon_{Rmax}^2 = \max \{ \varepsilon_R^2(\Theta) \}. \quad (20b)$$



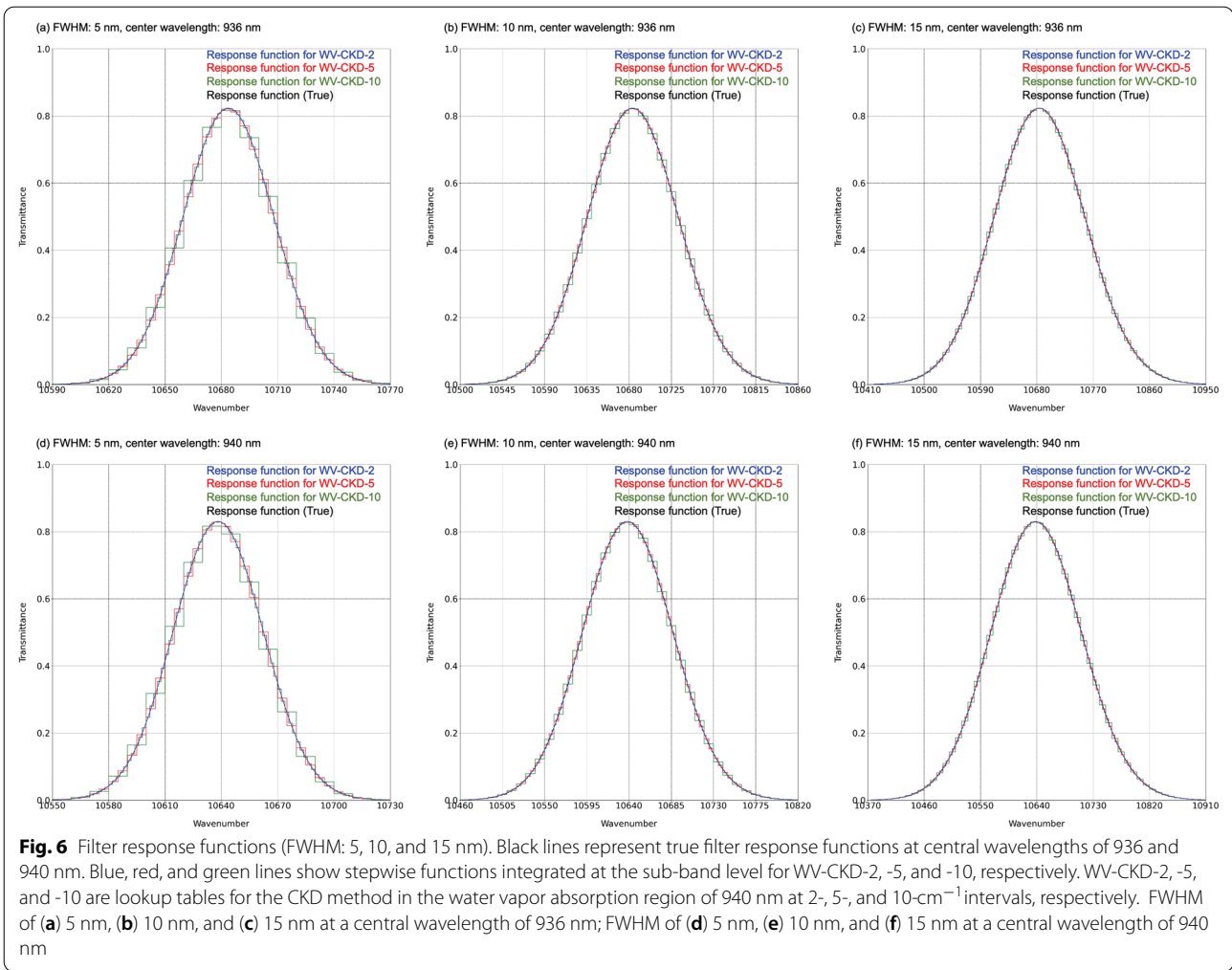


Figure 7 shows the angular distribution of the convolved normalized radiances simulated for type 2 DU-DB. Although the convolved \tilde{R} value obtained with the SN-CKD had large errors in backward scattering and the zenith region (approximately 1.5%), convolved \tilde{R} values from the WV-CKDs showed better performance (<0.1%). Table 5 summarizes $\varepsilon_{I_{\max}}^2$ and $\varepsilon_{R_{\max}}^2$ for the simulation using DU-DB. Although a finer Δ_{κ} is effective for assessing the shape of the filter response function, Table 5 does not follow this trend. This discrepancy arises because extraterrestrial solar irradiance has strong wavelength dependence (Coddington et al. 2021), so it might affect performance more strongly than the shape of the response function. In that case, the residual errors obtained with the WV-CKD-2 and WV-CKD-5 are within 3×10^{-3} . In the case of an FWHM of 5 nm, the residual errors from the WV-CKD-10 are significantly large ($>1 \times 10^{-2}$) due to the assumption of the stepwise function. In contrast, \tilde{R}^{CKD} was less strongly affected than \hat{T}^{CKD} and \hat{L}^{CKD}

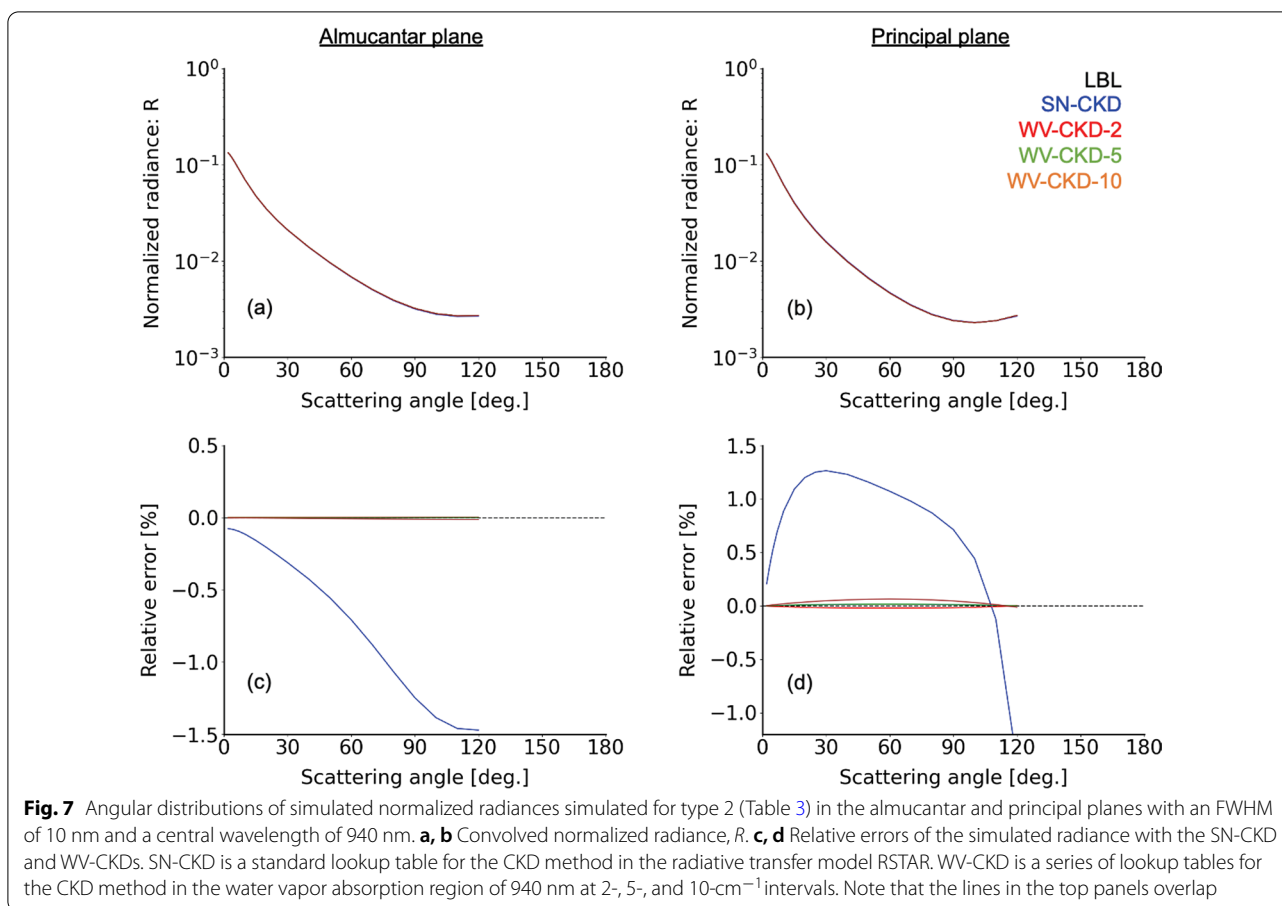
($\sqrt{\varepsilon_{R_{\max}}^2} \leq 1.1 \times 10^{-3}$), in accordance with the relationship between $\varepsilon_{R_{\max}}^2$ and $\varepsilon_{I_{\max}}^2$ described in Sect. 3.2.1. This finding indicates an advantage of sky-radiometer observations, as Momoi et al. (2020) proposed estimation of PWV from the angular distribution of \tilde{R} . With an FWHM of 10 nm, corresponding to the sky-radiometer specification, the $\sqrt{\varepsilon_{I_{\max}}^2}$ values of the WV-CKD-2, WV-CKD-5, and WV-CKD-10 are less than 3.2×10^{-3} , 1.3×10^{-3} , and 4.0×10^{-3} , respectively. These values are significantly smaller than $\sqrt{\varepsilon_{I_{\max}}^2}$ obtained using the SN-CKD ($\leq 1.5 \times 10^{-1}$). In comparison, the $\sqrt{\varepsilon_{R_{\max}}^2}$ values of all WV-CKDs reach 1.1×10^{-3} . In conclusion, this simulation suggests that the WV-CKD-5 is useful for computation of sky radiances (direct solar irradiances and normalized radiances) based on sky-radiometer observations. Moreover, this process is approximately 75-fold more rapid than the LBL method.

Table 4 Maximum residual errors of the convolved radiances assuming sub-band-averaged extraterrestrial solar irradiance and a filter response function. Residual errors larger than the expected residual values are underlined

FWHM (nm)	5					10					15								
	SN-CKD	WV-CKD-2	WV-CKD-5	WV-CKD-10	SN-CKD	SN-CKD	WV-CKD-2	WV-CKD-5	WV-CKD-10	SN-CKD	SN-CKD	WV-CKD-2	WV-CKD-5	WV-CKD-10	SN-CKD	SN-CKD	WV-CKD-2	WV-CKD-5	WV-CKD-10
<i>(a) 936 nm</i>																			
Type 1	ϵ_{rmax} ($\times 10^{-3}$)	221	0.451	0.205	0.063	145	0.165	0.022	0.140	110	0.173	0.117	0.193						
(ALM)	ϵ_{Rmax} ($\times 10^{-3}$)	12.7	0.016	0.053	0.024	8.13	0.005	0.019	0.062	7.00	0.002	0.014	0.071						
	ϵ_{rmax} ($\times 10^{-3}$)	221	0.451	0.331	0.063	145	0.375	0.071	0.140	110	0.421	0.169	0.193						
	ϵ_{Rmax} ($\times 10^{-3}$)	23.2	0.057	0.126	0.024	21.2	0.216	0.074	0.183	18.2	0.249	0.055	0.265						
Type 2	ϵ_{rmax} ($\times 10^{-3}$)	127	1.038	0.437	0.123	107	0.624	0.441	0.239	86.8	0.573	0.436	0.296						
(ALM)	ϵ_{Rmax} ($\times 10^{-3}$)	23.3	0.019	0.013	0.032	17.4	0.002	0.038	0.054	14.0	0.026	0.045	0.042						
	ϵ_{rmax} ($\times 10^{-3}$)	194	1.038	0.619	0.123	136	0.624	0.550	0.239	105	0.573	0.525	0.296						
	ϵ_{Rmax} ($\times 10^{-3}$)	67.1	0.397	0.183	0.046	28.8	0.265	0.109	0.065	18.0	0.169	0.089	0.105						
Type 3	ϵ_{rmax} ($\times 10^{-3}$)	93.2	1.470	0.512	0.214	7.58	1.213	0.311	0.218	17.9	1.000	0.249	0.178						
(ALM)	ϵ_{Rmax} ($\times 10^{-3}$)	14.4	0.005	0.035	0.002	11.9	0.043	0.048	0.037	8.19	0.067	0.065	0.052						
	ϵ_{rmax} ($\times 10^{-3}$)	93.2	1.470	0.541	0.214	43.2	1.213	0.405	0.218	41.8	1.006	0.329	0.178						
	ϵ_{Rmax} ($\times 10^{-3}$)	86.7	0.177	0.035	0.084	38.9	0.075	0.094	0.085	24.0	0.067	0.080	0.052						
Type 4	ϵ_{rmax} ($\times 10^{-3}$)	144	0.996	0.520	0.205	114	0.611	0.501	0.254	91.3	0.573	0.465	0.293						
(ALM)	ϵ_{Rmax} ($\times 10^{-3}$)	14.4	0.020	0.011	0.023	11.7	0.006	0.028	0.037	10.1	0.015	0.033	0.033						
	ϵ_{rmax} ($\times 10^{-3}$)	176	0.996	0.578	0.205	128	0.611	0.557	0.254	98.7	0.573	0.517	0.293						
(PPL)	ϵ_{Rmax} ($\times 10^{-3}$)	32.5	0.180	0.058	0.026	13.4	0.139	0.056	0.037	10.1	0.094	0.052	0.043						
Expected residual error ($\times 10^{-3}$)																			
$D\Phi(\epsilon_r^2)^{1/2}$																			
<i>(b) 940 nm</i>																			
Type 1	ϵ_{rmax} ($\times 10^{-3}$)	72.8	0.018	0.261	0.646	136	0.166	0.099	0.199	128	0.169	0.028	0.097						
(ALM)	ϵ_{Rmax} ($\times 10^{-3}$)	1.66	0.007	0.046	0.060	3.71	0.005	0.029	0.051	4.77	0.006	0.018	0.051						
	ϵ_{rmax} ($\times 10^{-3}$)	72.8	0.329	0.260	0.719	136	0.391	0.099	0.407	128	0.416	0.037	0.217						
	ϵ_{Rmax} ($\times 10^{-3}$)	24.0	0.347	0.112	0.073	28.2	0.230	0.052	0.208	25.6	0.253	0.047	0.263						
Type 2	ϵ_{rmax} ($\times 10^{-3}$)	80.0	0.472	0.228	0.185	127	0.631	0.275	0.157	116	0.573	0.324	0.236						
(ALM)	ϵ_{Rmax} ($\times 10^{-3}$)	11.5	0.033	0.044	0.039	14.8	0.019	0.024	0.029	15.3	0.002	0.028	0.033						
	ϵ_{rmax} ($\times 10^{-3}$)	85.3	0.472	0.506	0.185	140	0.631	0.378	0.216	130	0.573	0.356	0.235						
	ϵ_{Rmax} ($\times 10^{-3}$)	11.5	0.295	0.278	0.283	14.8	0.203	0.103	0.088	15.3	0.159	0.033	0.033						
Type 3	ϵ_{rmax} ($\times 10^{-3}$)	26.7	1.639	0.335	0.087	44.2	1.486	0.407	0.169	35.7	1.136	0.342	0.101						
(ALM)	ϵ_{Rmax} ($\times 10^{-3}$)	11.0	0.011	0.053	0.018	12.5	0.007	0.040	0.022	11.6	0.026	0.045	0.040						

Table 4 (continued)

FWHM (nm)	5			10			15					
	SN-CKD	WV-CKD-2	WV-CKD-5	SN-CKD	WV-CKD-2	WV-CKD-5	SN-CKD	WV-CKD-2	WV-CKD-5			
(PPL)	$\epsilon_{rmax} (\times 10^{-3})$	47.0	0.455	0.087	75.6	1.486	0.445	0.169	1.136	65.5	0.389	0.101
Type 4	$\epsilon_{Rmax} (\times 10^{-3})$	20.3	0.119	0.018	31.4	0.104	0.040	0.022	0.039	29.8	0.048	0.040
(ALM)	$\epsilon_{rmax} (\times 10^{-3})$	80.3	0.374	0.013	130	0.638	0.331	0.277	0.573	119	0.346	0.296
(PPL)	$\epsilon_{Rmax} (\times 10^{-3})$	7.72	0.030	0.021	9.73	0.020	0.016	0.016	0.006	10.3	0.018	0.022
Expected residual error ($\times 10^{-3}$)	$\epsilon_{rmax} (\times 10^{-3})$	81.9	0.497	0.121	136	0.638	0.382	0.300	0.573	126	0.369	0.296
$D\Phi(\epsilon_E^2)^{1/2}$	$\epsilon_{Rmax} (\times 10^{-3})$	7.72	0.123	0.129	9.73	0.102	0.051	0.039	0.083	10.3	0.024	0.022
		2.0			1.4					1.1		



3.3 Relationship between convolved normalized radiances around 940 nm and PWV

Momoi et al. (2020) investigated the relationships among \bar{R} around 940 nm, PWV, and the vertical profiles of aerosols and reported two major findings. First, \bar{R} depends on PWV in both almucantar and principal planes, with \bar{R} in the principal plane being more strongly dependent on PWV. Second, \bar{R} in the principal plane depends on the vertical aerosol profile, whereas \bar{R} in the almucantar plane is nearly independent of the vertical aerosol profile. Because Momoi et al. (2020) used the SN-CKD, we repeated their analysis with the WV-CKD-2. In this section, we describe sensitivity tests conducted under two aerosol conditions with US standard atmospheres, as described by Momoi et al. (2020): the continental average and the continental average + transported dust in the upper atmosphere (Table 6). All continental average aerosols were assumed to be spherical, and the dust aerosols were assumed to be spheroid, which differed from the assumption used in Momoi et al. (2020). The spheroid particles used here are the kernels developed by Dubovik et al. (2006) with an aspect ratio set to 0.6,

representing the yellow sand particles reported by Nakajima et al. (1989). The radiances were convolved with a filter response function of Gaussian shape with an FWHM of 10 nm and central wavelength of 940 nm. Note that the filter response function also differed from the function described by Momoi et al. (2020).

Figure 8 shows the results of sensitivity tests conducted with the SN-CKD and WV-CKD-2. The results obtained with the SN-CKD are similar to those described by Momoi et al. (2020). Although the magnitude of \bar{R} differed from the value reported by Momoi et al. (2020), the relationship between \bar{R} around 940 nm and PWV was consistent with their findings. Other sensitivity tests (Figs. 4–6 in Momoi et al. 2020) had the same characteristic.

3.4 PWV estimation from sky-radiometer observations

3.4.1 Brief outline of the method proposed by Momoi et al. (2020)

According to Momoi et al. (2020), the calibration constants for the water vapor band (940 nm) can be determined using \bar{T} derived from the angular distribution of \bar{R} ,

Table 5 As described for Table 4, but the reference radiances were computed with a smooth filter response function and the high-resolution (0.01cm⁻¹) extraterrestrial solar irradiance data

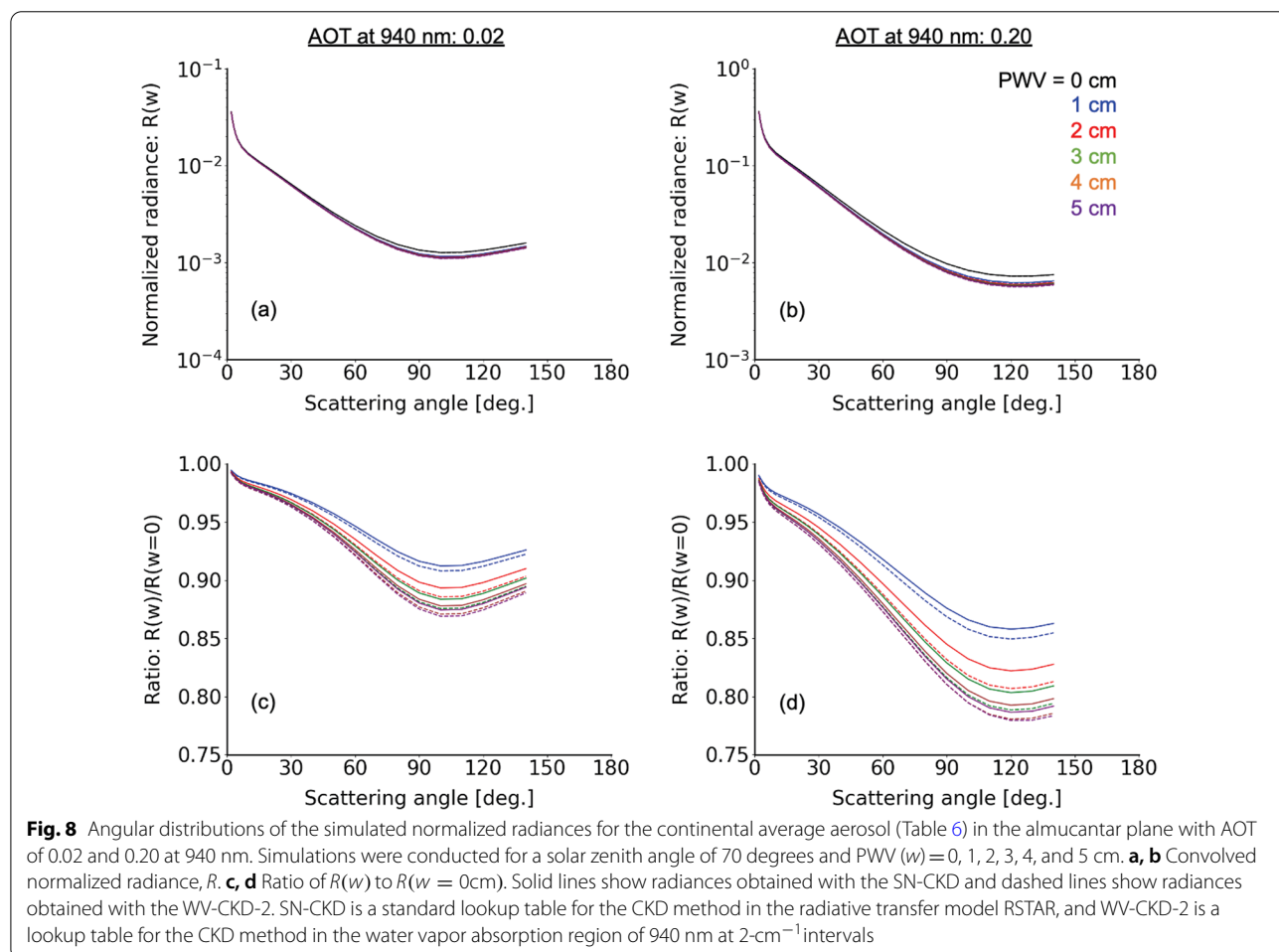
Database	5			10			15			
	SN-CKD	WV-CKD-2	WV-CKD-5	SN-CKD	WV-CKD-2	WV-CKD-5	SN-CKD	WV-CKD-2	WV-CKD-5	
<i>(a) 936 nm</i>										
Type 1	ϵ_{lmax} ($\times 10^{-3}$)	0.247	0.961	5.043	1.740	0.398	0.919	1.521	0.246	0.772
(ALM)	ϵ_{Rmax} ($\times 10^{-3}$)	0.108	0.090	0.053	0.471	0.355	0.506	0.309	0.189	0.308
(PPL)	ϵ_{lmax} ($\times 10^{-3}$)	0.247	0.961	5.038	1.740	0.398	0.919	1.521	0.295	0.772
Type 2	ϵ_{Rmax} ($\times 10^{-3}$)	0.169	0.221	0.422	0.531	0.355	0.602	0.492	0.189	0.417
(ALM)	ϵ_{lmax} ($\times 10^{-3}$)	1.569	1.905	4.271	2.706	0.631	2.850	1.871	0.523	1.286
(PPL)	ϵ_{Rmax} ($\times 10^{-3}$)	0.162	0.162	0.061	0.523	0.371	0.390	0.251	0.114	0.119
Type 3	ϵ_{lmax} ($\times 10^{-3}$)	1.569	1.905	4.588	2.706	0.631	2.850	1.871	0.610	1.286
(ALM)	ϵ_{Rmax} ($\times 10^{-3}$)	0.808	0.178	0.379	0.523	0.395	1.058	0.251	0.114	0.359
(PPL)	ϵ_{lmax} ($\times 10^{-3}$)	2.897	2.402	2.901	3.153	1.197	3.982	1.728	0.555	1.158
Type 4	ϵ_{Rmax} ($\times 10^{-3}$)	0.093	0.119	0.168	0.468	0.325	0.160	0.161	0.110	0.077
(ALM)	ϵ_{lmax} ($\times 10^{-3}$)	2.897	2.402	3.330	3.153	1.197	3.982	1.728	0.555	1.104
(PPL)	ϵ_{Rmax} ($\times 10^{-3}$)	0.570	0.185	0.597	0.468	0.325	0.514	0.161	0.073	0.024
Type 5	ϵ_{lmax} ($\times 10^{-3}$)	1.378	1.807	4.176	2.339	0.353	2.521	1.647	0.655	1.189
(ALM)	ϵ_{Rmax} ($\times 10^{-3}$)	0.108	0.113	0.128	0.435	0.342	0.319	0.215	0.171	0.154
(PPL)	ϵ_{lmax} ($\times 10^{-3}$)	1.378	1.807	4.375	2.339	0.353	2.521	1.643	0.655	1.159
Expected residual error ($\times 10^{-3}$)	ϵ_{Rmax} ($\times 10^{-3}$)	0.363	0.113	0.327	0.435	0.342	0.345	0.211	0.130	0.124
<i>(b) 940 nm</i>										
Type 1	$D\Phi(\epsilon_E^2)^{1/2}$	2.0	2.0	1.4	1.4	1.1	1.1	1.1	1.1	1.1
(ALM)	ϵ_{lmax} ($\times 10^{-3}$)	0.369	0.190	11.72	0.767	1.078	1.333	1.494	0.549	0.357
(PPL)	ϵ_{Rmax} ($\times 10^{-3}$)	0.075	0.210	0.761	0.160	0.142	0.305	0.242	0.184	0.262
Type 2	ϵ_{lmax} ($\times 10^{-3}$)	0.878	0.695	11.72	0.767	1.133	1.333	1.494	0.597	0.357
(ALM)	ϵ_{Rmax} ($\times 10^{-3}$)	0.509	0.504	2.463	0.394	0.142	0.685	0.468	0.184	0.403
(PPL)	ϵ_{lmax} ($\times 10^{-3}$)	0.317	0.724	16.77	0.942	1.152	2.875	1.855	0.686	1.019
Type 3	ϵ_{Rmax} ($\times 10^{-3}$)	0.048	0.148	0.378	0.182	0.164	0.242	0.277	0.205	0.227
(ALM)	ϵ_{lmax} ($\times 10^{-3}$)	0.333	0.724	16.77	0.942	1.369	2.875	1.855	0.808	1.019
(PPL)	ϵ_{Rmax} ($\times 10^{-3}$)	0.047	0.857	2.323	0.182	0.217	0.505	0.277	0.205	0.233
Type 4	ϵ_{lmax} ($\times 10^{-3}$)	1.034	1.417	19.19	0.648	0.936	3.572	1.848	0.536	1.113
(ALM)	ϵ_{Rmax} ($\times 10^{-3}$)	0.049	0.114	0.134	0.171	0.173	0.213	0.256	0.190	0.202
(PPL)	ϵ_{lmax} ($\times 10^{-3}$)	1.077	1.417	19.19	0.648	1.022	3.572	1.848	0.566	1.113

Table 5 (continued)

Database	5			10			15					
	SN-CKD	WV-CKD-2	WV-CKD-5	SN-CKD	WV-CKD-2	WV-CKD-5	SN-CKD	WV-CKD-2	WV-CKD-5			
(PPL)	$\epsilon_{rmax} (\times 10^{-3})$	20.1	0.339	0.807	31.2	0.171	0.173	0.213	29.7	0.256	0.190	0.202
Type 4	$\epsilon_{rmax} (\times 10^{-3})$	93.5	0.466	16.35	134	0.767	1.265	2.839	120	1.647	0.809	0.966
(ALM)	$\epsilon_{rmax} (\times 10^{-3})$	7.82	0.017	0.279	9.72	0.130	0.140	0.206	10.2	0.218	0.187	0.211
(PPL)	$\epsilon_{rmax} (\times 10^{-3})$	94.6	0.466	16.35	140	0.754	1.305	2.827	127	1.634	0.809	0.945
Expected residual error ($\times 10^{-3}$)	ϵ_{rmax}	7.82	0.017	0.357	9.72	0.117	0.124	0.194	10.2	0.205	0.167	0.190
$D(\epsilon_E^2)^{1/2}$		2.0				1.4				1.1		

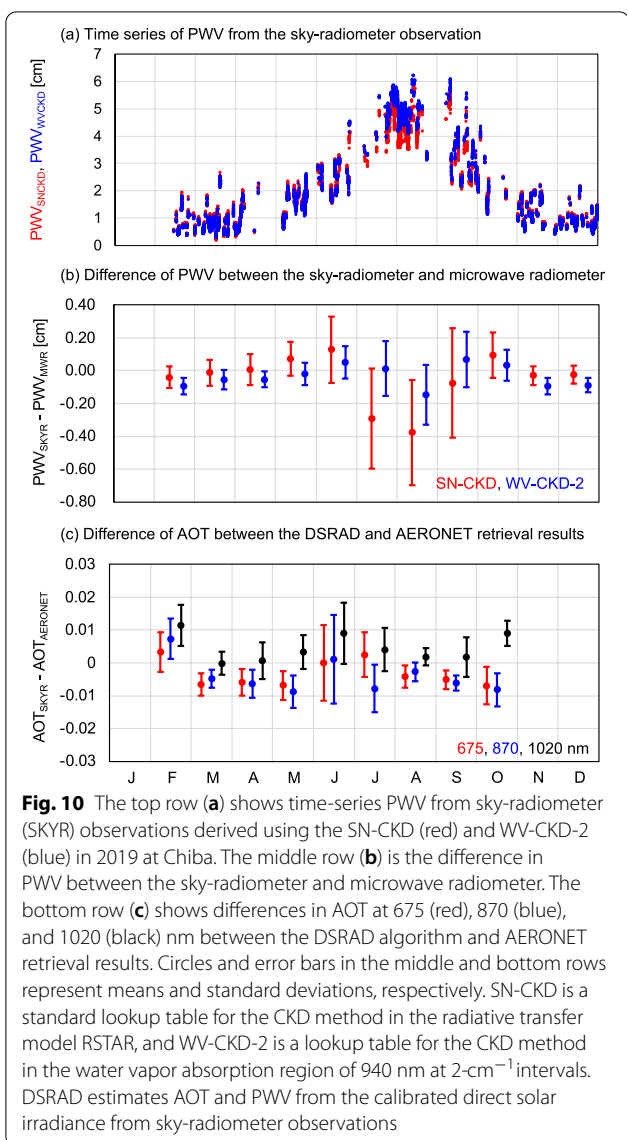
Table 6 Microphysical and optical properties and vertical profiles of aerosols used in sensitivity testing, in accordance with the approach described by Momoi et al. (2020)

Aerosol	Components	Size distribution		Refractive index at 940 nm		Relative weight in total optical thickness at 500 nm	Vertical profile
		Mode radius (μm)	Mode width	Real	Imaginary		
Continental average	Water-soluble	0.18	0.81	1.43	0.0074	0.90	$\exp(-z/H), H=8$ km
	Soot	0.05	0.69	1.75	0.44	0.07	$\exp(-z/H), H=4$ km
	Insoluble	5.98	0.92	1.52	0.008	0.03	$\exp(-z/H), H=2$ km
Transported dust	Dust	3.23	0.79	1.53	0.004	0.25	$\frac{1}{\sqrt{2\pi}\sigma} \exp\left(-\frac{(z-z_c)^2}{2\sigma^2}\right), z_c=3.5$ km $\sigma=0.4$ km
	Water-soluble	0.18	0.81	1.43	0.0074	0.67	$\exp(-z/H), H=8$ km
	Soot	0.05	0.69	1.75	0.44	0.05	$\exp(-z/H), H=4$ km
	Insoluble	5.98	0.92	1.52	0.008	0.03	$\exp(-z/H), H=2$ km



which is referred to as the SKYMAP algorithm. The SKYMAP algorithm includes the following three steps (Fig. 9). Aerosol properties (aerosol size distribution, complex

refractive index, and sphericity) are estimated from the angular distribution of \tilde{R} in the range of 340–1020 nm, except at 940 nm; \tilde{T} at 940 nm is estimated from the



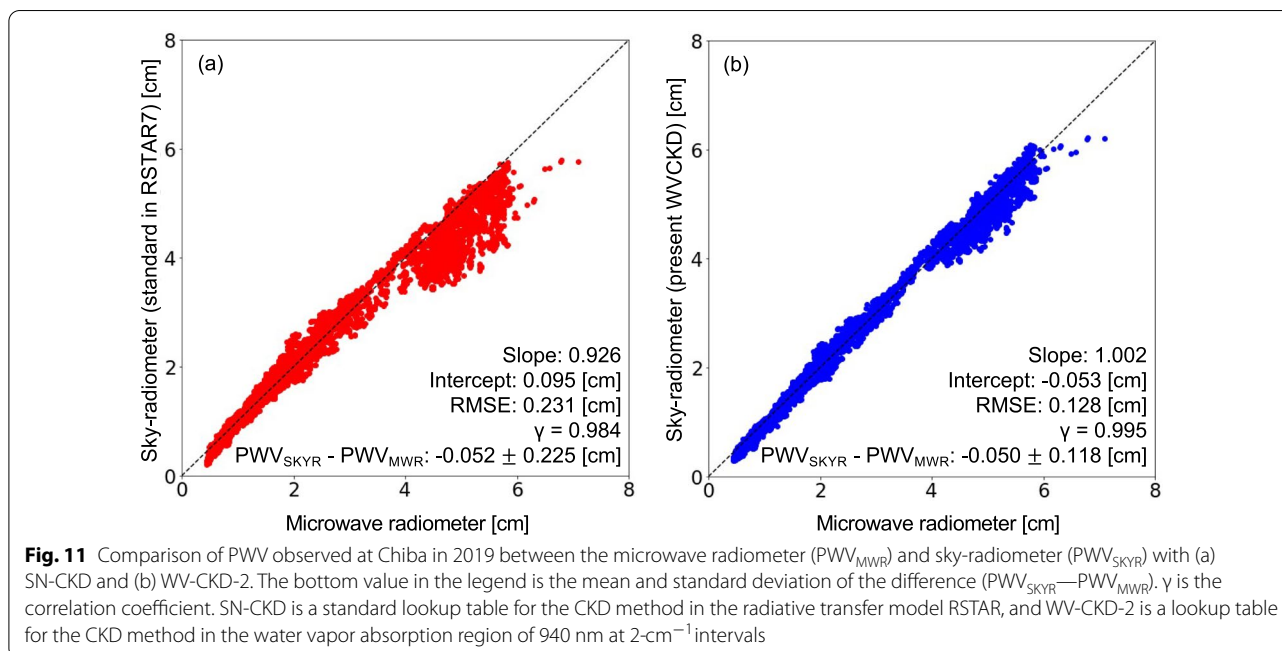
AERONET photometer reached 0.01, corresponding to an absolute PWV error of about 0.08 cm calculated using the equation of Momoi et al. (2020). In contrast, the PWV_{SNCKD} errors larger than 0.08 cm shown in Fig. 10b are considered to represent the errors in PWV arising from the SN-CKD, rather than from the uncertainty in AOT estimation. This suggests that SKYMAP/DSRAD calculation with the WV-CKD is useful for accurate estimation of PWV and determination of the calibration constant \tilde{F}_0 for the water vapor absorption band of sky-radiometer observations.

4 Conclusions

To compute direct solar irradiance and diffuse radiance at ground level around 940 nm with narrow-band RTMs, we developed a rapid calculation module using

a LUT (WV-CKD). We found the challenges facing the currently used LUT (SN-CKD) in RSTAR7 for narrow-band sky radiance computation around 940 nm region. As shown by comparison of the sky intensities of sub-bands obtained with the LBL method and CKD method using the SN-CKD, the root mean square error of the maximum error in sub-bands obtained with the SN-CKD is 116% across the range of 10,411–10,864 cm⁻¹ [961–920 nm]. This large error may arise from the updated database and lack of optimization. Our WV-CKDs were created at three different spectral resolutions ($\Delta_\kappa = 2, 5, 10\text{cm}^{-1}$ in WV-CKD-2, WV-CKD-5, and WV-CKD-10, respectively). The quadrature values and numbers of these WV-CKDs were optimized using sky intensities based on the single-scattering approximation at ground level, with an accuracy of $\leq 0.5\%$ for sub-bands of 10cm⁻¹. The quadrature numbers affected computational efficiency. The median quadrature numbers of WV-CKD-2, WV-CKD-5, and WV-CKD-10 are 4, 6, and 7, respectively; their calculations were ≥ 46 -fold more rapid than the LBL method.

Radiance calculation with the WV-CKD was evaluated for two aerosol types and four vertical profiles that differed from the conditions used for optimization of the tables. The residual errors of convolved sky intensities (\hat{T}^{CKD} and \hat{L}^{CKD}) were similar to the expected errors observed during optimization of quadrature values and numbers. This finding suggests that the WV-CKD has sufficient versatility for application under actual atmospheric conditions. The convolved normalized radiance (\hat{R}^{CKD}) was less strongly affected by residual errors obtained using the WV-CKD than \hat{T}^{CKD} and \hat{L}^{CKD} , as \hat{R}^{CKD} cancels the residual errors of both \hat{T}^{CKD} and \hat{L}^{CKD} . Additionally, while the error of convolved sky intensities obtained with the SN-CKD is within 15%, use of WV-CKD provides convolved sky intensities with an accuracy of $\leq 0.3\%$ at an FWHM of 10 nm, equal to the FWHM of the sky-radiometer. This accuracy is lower than the PWV dependence on \tilde{R} and measurement uncertainty (approximately 0.5%). Finally, we applied the SKYMAP and DSRAD algorithms (Momoi et al. 2020) to SKYNET observations and compared the results with those of the microwave radiometer. PWV shows better agreement when derived with the WV-CKD (correlation coefficient $\gamma = 0.995$, slope = 1.002) than with the SN-CKD (correlation coefficient $\gamma = 0.984$, slope = 0.926), as used by Momoi et al. (2020). Therefore, through application of the WV-CKD to actual data analysis, we demonstrated that an accurate CKD table is essential for estimating PWV from sky-radiometer observations.



Abbreviations

RTM: Radiative transfer model; LUT: Lookup table; RSTAR: System for Transfer of Atmospheric Radiation for Radiance calculations; PSTAR: System for Transfer of Atmospheric Radiation for Polarized radiance calculations; CKD: Correlated k -distribution; SN-CKD: Standard lookup table for the correlated k -distribution method in RSTAR; RSTAR7: RSTAR version 7; PSTAR4: PSTAR version 4; PWV: Precipitable water vapor; AERONET: Aerosol robotic network; LBL: Line-by-line; AFGL: Air Force Geophysics Laboratory; WV-CKD: Lookup table for the correlated k -distribution method in the water vapor absorption region of 940 nm; CA-DB: Dataset consisting of radiances at ground level under continental averaged aerosol condition; AOT: aerosol optical thickness, FWHM: Full width at half maximum; DU-DB: Dataset consisting of the radiances at ground level under several aerosol conditions from Dubovik et al. (2000); MWR: Microwave radiometer.

Acknowledgements

We are grateful to the OpenCLASTR project (<http://157.82.240.167/~clastr/>, last accessed: Oct. 2021) for allowing us to use SKYRAD.pack version 4.2 (sky-radiometer analysis package) and RSTAR7 (System for Transfer of Atmospheric Radiation for Radiance calculations) in this study. NCEP reanalysis 1 data were obtained from the website of the National Oceanic & Atmospheric Administration (NOAA) Earth System Research Laboratory (ESRL) Physical Sciences Division (PSD; Boulder, CO, USA) at <http://www.esrl.noaa.gov/psd/> (last accessed: Oct. 2021).

Authors' contributions

This study was designed by MM and HI. The gas absorption calculation modules for RSTAR7 and the WV-CKDs were developed by MM, TN, and MS. The sky-radiometer data were analyzed by MM, HI, KM, and KA. The sky-radiometer (S/N PS2501401) was maintained by MM, KM, and KA. The sky-radiometer (S/N PS2501417) and microwave radiometer were maintained by HI. The high-performance computers used for analysis were operated and maintained by MM and HT. The manuscript was written by MM, and all authors contributed to its editing and revision. All authors read and approved the final manuscript.

Funding

This study was partly supported by the Environment Research and Technology Development Fund (JPMEERF20192001 and JPMEERF20215005) of the Environmental Restoration and Conservation Agency of Japan, JSPS KAKENHI (Grant Numbers JP19H04235, JP20H04320, and JP21K12227), the

JAXA 2nd research announcement on the Earth Observations (Grant Number 19RT000351), a Tokyo University of Science Joint Research Grant (Representative Kazuhiko Miura, 2013-2014), and JAXA Contract research ("Fundamental development of radiative transfer codes for advanced utilization of earth observation satellites," FY2021).

Availability of data and materials

RSTAR and PSTAR are available from the OpenCLASTR project website (<http://157.82.240.167/~clastr/>, last accessed: Oct. 2021). The LUTs around 940 nm (WV-CKDs) and gas absorption calculation codes for RSTAR7 and PSTAR4 are available on request from the first author. The SKYMAP and DSRAD algorithms are also available on request from the first author. The sky-radiometer data are available from the SKYNET website (<http://www.skynet-isdc.org/>, last accessed: Oct. 2021). The MWR data are available from CERES, Chiba University (<http://atmos3.cr.chiba-u.jp/skynet/>, last accessed: Oct. 2021). The AERONET sun-sky radiometer data are available from the AERONET website (<https://aeronet.gsfc.nasa.gov/>, last access: Oct. 2021).

Declarations

Competing interests

The authors declare that they have no competing interest.

Author details

¹Center for Environmental Remote Sensing, Chiba University, 1-33 Yayoicho, Inage-ku, Chiba 263-8522, Japan. ²Faculty of Marine Technology, Tokyo University of Marine Science and Technology, 2-1-6 Etchujima, Koto-ku, Tokyo 135-8533, Japan. ³National Institute for Environmental Studies, 16-2 Onogawa, Tsukuba, Ibaraki 305-8506, Japan. ⁴Department of Physics, Faculty of Science Division I, Tokyo University of Science, 1-3 Kagurazaka, Shinjuku-ku, Tokyo 162-8601, Japan. ⁵Laboratory for Environmental Research at Mount Fuji, 2-5-5 Okubo, Shinjuku-ku, Tokyo 169-0072, Japan. ⁶Graduate School of Science and Engineering, University of Toyama, 3190 Gofuku, Toyama, Toyama 930-8555, Japan.

Received: 12 August 2021 Accepted: 7 January 2022

Published online: 28 January 2022

References

- Boi P, Tonna G, Dalu G, Nakajima T, Olivieri B, Pompei A, Campanelli M, Rao R (1999) Calibration and data elaboration procedure for sky irradiance measurements. *Appl Opt* 38(6):896–907
- Bojinski S, Verstraete M, Peterson TC, Richter C, Simmons A, Zemp M (2014) The concept of essential climate variables in support of climate research, applications, and policy. *Bull Am Meteor Soc* 95(9):1431–1443. <https://doi.org/10.1175/BAMS-D-13-00047.1>
- Bruegge CJ, Conel JE, Green RO, Margolis JS, Holm RG, Roon G (1992) Water vapor column abundance retrievals during FIFE. *J Geophys Res* 97:18759–18768
- Campanelli M, Nakajima T, Khatri P, Takamura T, Uchiyama A, Estellés V, Liberti GL, Malvestuto V (2014) Retrieval of characteristic parameters for water vapour transmittance in the development of ground-based sun-sky radiometric measurements of columnar water vapour. *Atmos Meas Tech* 7:1075–1087
- Campanelli M, Mascitelli A, Sanò P, Diémoz H, Estellés V, Federico S, Iannarelli AM, Fratarcangeli F, Mazzoni A, Realini E, Crespi M, Bock O, Martínez-Lozano JA, Dietrich S (2018) Precipitable water vapour content from ESR/SKYNET sun-sky radiometers: validation against GNSS/GPS and AERONET over three different sites in Europe. *Atmos Meas Tech* 11:81–94
- Coddington OM, Richard EC, Harber D, Pilewskie P, Woods TN, Chance K, Liu X, Sun K (2021) The TSIS-1 hybrid solar reference spectrum. *Geophys Res Lett* 48:e2020GL091709. <https://doi.org/10.1029/2020GL091709>
- Dubovik O, Smirnov A, Holben BN, King MD, Kaufman YJ, Eck TF, Slutsker I (2000) Accuracy assessments of aerosol optical properties retrieved from Aerosol Robotic Network (AERONET) Sun and sky radiance measurements. *J Geophys Res* 105:9791–9806
- Dubovik O, King MD (2000) A flexible inversion algorithm for retrieval of aerosol optical properties from sun and sky radiance measurements. *J Geophys Res* 105:20673–20696
- Dubovik O, Sinyuk A, Lapyonok T, Holben BN, Mishchenko M, Yang P, Eck TF, Volte H, Muñoz O, Veihelmann B, van der Zande WJ, Leon J-F, Sorokin M, Slutsker I (2006) Application of spheroid models to account for aerosol particle nonsphericity in remote sensing of desert dust. *J Geophys Res* 111:D11208. <https://doi.org/10.1029/2005JD006619>
- Dubovik O, Herman M, Holdak A, Lapyonok T, Tanré D, Deuzé JL, Ducos F, Sinyuk A, Lopatin A (2011) Statistically optimized inversion algorithm for enhanced retrieval of aerosol properties from spectral multi-angle polarimetric satellite observations. *Atmos Meas Tech* 4:975–1018
- Fowle FE (1912) The spectroscopic determination of aqueous vapor. *Astrophys J* 35:149–162
- Fowle FE (1915) The transparency of aqueous vapor. *Astrophys J* 42:394–411
- Fu Q, Liou KN (1992) On the correlated k-distribution method for radiative transfer in nonhomogeneous atmospheres. *J Atmos Sci* 49:2139–2156
- Giles DM, Sinyuk A, Sorokin MG, Schafer JS, Smirnov A, Slutsker I, Eck TF, Holben BN, Lewis JR, Campbell JR, Welton EJ, Korkin SV, Lyapustin AI (2019) Advancements in the Aerosol Robotic Network (AERONET) Version 3 database—automated near-real-time quality control algorithm with improved cloud screening for Sun photometer aerosol optical depth (AOD) measurements. *Atmos Meas Tech* 12:169–209. <https://doi.org/10.5194/amt-12-169-2019>
- Halthore RN, Eck TF, Holben BN, Markham BL (1997) Sun photometric measurements of atmospheric water vapor column abundance in the 940-nm band. *J Geophys Res* 102:4343–4352
- Hashimoto M, Nakajima T, Dubovik O, Campanelli M, Che H, Khatri P, Takamura T, Pandithurai G (2012) Development of a new data-processing method for SKYNET sky radiometer observations. *Atmos Meas Tech* 5:2723–2737
- Hashimoto M, Nakajima T (2017) Development of a remote sensing algorithm to retrieve atmospheric aerosol properties using multiwavelength and multipixel information. *J Geophys Res Atmos*. <https://doi.org/10.1002/2016JD025698>
- Hess M, Koepke P, Schult I (1999) Optical properties of aerosols and clouds: the software package OPAC. *B Am Meteorol Soc* 79:831–844
- Holben BN, Eck TF, Slutsker I, Tanré D, Buis JP, Setzer A, Vermote E, Reagan JA, Kaufman YJ, Nakajima T, Lavenu F, Jankowiak I, Smirnov A (1998) AERONET—A federated instrument network and data archive for aerosol characterization. *Remote Sens Environ* 66:1–16
- IPCC (2021) Summary for Policymakers. In: Masson-Delmotte V, Zhai P, Pirani A, Connors SL, Péan C, Berger S, Caud N, Chen Y, Goldfarb L, Gomis MI, Huang M, Leitzell K, Lonnoy E, Matthews JBR, Maycock TK, Waterfield T, Yelekçi O, Yu R, Zhou B (eds.) *Climate Change 2021: The Physical Science Basis. Contribution of Working Group I to the Sixth Assessment Report of the Intergovernmental Panel on Climate Change*. Cambridge University Press (In Press)
- Khatri P, Takamura T, Yamazaki A, Uchiyama A (2014) Use of 315 nm channel data of the sky radiometer to estimate the columnar ozone concentration: a preliminary study. *J Meteorol Soc Jpn* 92A:185–194. <https://doi.org/10.2151/jmsj.2014-A12>
- Khatri P, Iwabuchi H, Hayasaka T, Irie H, Takamura T, Yamazaki A, Damiani A, Letu H, Kai Q (2019) Retrieval of cloud properties from spectral zenith radiances observed by sky radiometers. *Atmos Meas Tech* 12:6037–6047. <https://doi.org/10.5194/amt-12-6037-2019>
- Korkin S, Lyapustin A, Sinyuk A, Holben BN, Kokhanovsky A (2017) Vector radiative transfer code SORD: performance analysis and quick start guide. *J Quant Spectrosc Ra* 200:295–310
- Kudo R, Diémoz H, Estellés V, Campanelli M, Momoi M, Marengo F, Ryder C, Ijima O, Uchiyama A, Nakashima K, Yamazaki A, Nagawasa R, Ohkawara N, Ishida H (2021) Optimal use of the Prede POM sky radiometer for aerosol, water vapor, and ozone retrievals. *Atmos Meas Tech* 14:3395–3426. <https://doi.org/10.5194/amt-14-3395-2021>
- Lacis AA, Oinas VA (1991) Description of the correlated k-distribution method for modeling nongray gaseous absorption, thermal emission, and multiple scattering in vertically inhomogeneous atmospheres. *J Geophys Res* 96:9027–9063
- Mlawer EJ, Payne VH, Moncet J, Delamere JS, Alvarado MJ, Tobin DC (2012) Development and recent evaluation of the MT_CKD model of continuum absorption. *Phil Trans R Soc A* 370:2520–2556. <https://doi.org/10.1098/rsta.2011.0295>
- Momoi M, Kudo R, Aoki K, Mori T, Miura K, Okamoto H, Irie H, Shoji Y, Uchiyama A, Ijima O, Takano M, Nakajima T (2020) Development of on-site self-calibration and retrieval methods for sky-radiometer observations of precipitable water vapor. *Atmos Meas Tech* 13:2635–2658. <https://doi.org/10.5194/amt-13-2635-2020>
- Momoi M, Irie H, Nakajima T, Sekiguchi M (2022) Efficient calculation of radiative intensity including the polarization effect in moderately thick atmospheres using a truncation approximation. *J Quant Spectrosc Radiat Transf* 277:107976. <https://doi.org/10.1016/j.jqsrt.2021.107976>
- Nakajima T, Tanaka M (1986) Matrix formulations for the transfer of solar radiation in a plane-parallel scattering atmosphere. *J Quant Spectrosc Radiat Transf* 35:13–21
- Nakajima T, Tanaka M (1988) Algorithms for radiative intensity calculations in moderately thick atmospheres using a truncation approximation. *J Quant Spectrosc Radiat Transf* 40:51–69
- Nakajima T, Tanaka M, Yamano M, Shiobara M, Arai K, Nakanishi Y (1989) Aerosol optical characteristics in the yellow sand events observed in May, 1982 at Nagasaki-Part II models. *J Meteorol Soc Jpn* 67:279–291. https://doi.org/10.2151/jmsj1965.67.2_279
- Nakajima T, Tonna G, Rao R, Boi P, Kaufman Y, Holben B (1996) Use of Sky brightness measurements from ground for remote sensing of particulate polydispersions. *Appl Opt* 35:2672–2686
- Nakajima T, Tsukamoto M, Tsushima Y, Numaguti A, Kimura T (2000) Modeling of the radiative process in an atmospheric general circulation model. *Appl Opt* 39:4869–4878. <https://doi.org/10.1364/AO.39.004869>
- Nakajima T, Yoon SC, Ramanathan V, Shi GY, Takemura T, Higurashi A, Takamura T, Aoki K, Sohn BJ, Kim SW, Tsuruta H, Sugimoto N, Shimizu A, Tanimoto H, Sawa Y, Lin NH, Lee CT, Goto D, Schutgens N (2007) Overview of the atmospheric brown cloud east Asia regional experiment 2005 and a study of the aerosol direct radiative forcing in east Asia. *J Geophys Res* 112:D24591. <https://doi.org/10.1029/2007JD009009>
- Nakajima T, Campanelli M, Che H, Estellés V, Irie H, Kim S, Kim J, Liu D, Nishizawa T, Pandithurai G, Soni VK, Thana B, Tugjurn N, Aoki K, Go S, Hashimoto M, Higurashi A, Kazadzis S, Khatri P, Kouremeti N, Kudo R, Marengo F, Momoi M, Ningombam SS, Royder CL, Uchiyama A, Yamazaki A (2020) An overview of and issues with sky radiometer technology and SKYNET. *Atmos Meas Tech* 13:4195–4218. <https://doi.org/10.5194/amt-13-4195-2020>
- Ota Y, Higurashi A, Nakajima T, Yokota T (2010) Matrix formulations of radiative transfer including the polarization effect in a coupled atmosphere–ocean system. *J Quant Spectrosc Radiat Transf* 111:878–894
- Rodgers CD (2000) *Inverse method for atmospheric sounding*. World Science, Singapore

- Rothman LSD, Jacquemart A, Barbe DC, Benner MB, Brown LR, Carleer MR, Chackerian C Jr, Chance K, Coudert LH, Dana V, Devi VM, Flaud J-M, Gamache RR, Goldman A, Hartmann J-M, Jucks KW, Maki AG, Mandin J-Y, Massie ST, Orphal J, Perrin A, Rinsland CP, Smith MAH, Tennyson J, Tolchenov RN, Toth RA, Vander Auwera J, Varanasi P, Wagner G (2005) The HITRAN 2004 molecular spectroscopic database. *J Quant Spectrosc Radiat Transf* 96(2):139–204. <https://doi.org/10.1016/j.jqsrt.2004.10.008>
- Rothman LS, Gordon IE, Babikov Y, Barbe A, Chris Benner D, Bernath PF, Birk M, Bizzocchi L, Boudon V, Brown LR, Campargue A, Chance K, Cohen EA, Coudert LH, Devi VM, Drouin BJ, Fayt A, Flaud J-M, Gamache RR, Harrison JJ, Hartmann J-M, Hill C, Hodges JT, Jacquemart D, Jolly A, Lamouroux J, Le Roy RJ, Li G, Long DA, Lyulin OM, Mackie CJ, Massie ST, Mikhailenko S, Müller HSP, Naumenko OV, Nikitin AV, Orphal J, Perevalov V, Perrin A, Polovtseva ER, Richard C, Smith MAH, Starikova E, Sung K, Tashkun S, Tennyson J, Toon GC, Vi G, Tyuterev GW (2013) The HITRAN2012 molecular spectroscopic database. *J Quant Spectrosc Radiat Transf* 130:4–50. <https://doi.org/10.1016/j.jqsrt.2013.07.002>
- Schmid B, Thome KJ, Demoulin P, Peter R, Matzler C, Sekler J (1996) Comparison of modeled and empirical approaches for retrieving columnar water vapor from solar transmittance measurements in the 0.94-mm region. *J Geophys Res* 101:9345–9358
- Schmid B, Michalsky JJ, Slater DW, Barnard JC, Halthore RN, Liljegren JC, Holben BN, Eck TF, Livingston JM, Russell PB, Ingold T, Slutsker I (2001) Comparison of columnar water-vapor measurements from solar transmittance methods. *Appl Opt* 40:1886–1896
- Sekiguchi M, Nakajima T (2008) A k-distribution-based radiation code and its computational optimization for an atmospheric general circulation model. *J Quant Spectrosc Radiat Transf* 109:2779–2793
- Sekiguchi M, Iwabuchi H, Nagao TM, Nakajima T (2018) Development of gas absorption tables and an atmospheric radiative transfer package for applications using the advanced Himawari imager. *J Meteorol Soc Jpn* 96B:77–89. <https://doi.org/10.2151/jmsj.2018-007>
- Shi C, Hashimoto M, Nakajima T (2019) Remote sensing of aerosol properties from multi-wavelength and multi-pixel information over the ocean. *Atmos Chem Phys* 19:2461–2475
- Sinyuk A, Holben BN, Eck TF, Giles DM, Slutsker I, Korkin S, Schafer JS, Smirnov A, Sorokin M, Lyapustin A (2020) The AERONET Version 3 aerosol retrieval algorithm, associated uncertainties and comparisons to Version 2. *Atmos Meas Tech* 13:3375–3411. <https://doi.org/10.5194/amt-13-3375-2020>
- Takamura T, Nakajima T (2004) Overview of SKYNET and its activities. *Proc AERONET Work Pt Pura y Apl* 37:3303–3308
- Takenaka H, Nakajima TY, Higurashi A, Higuchi A, Takamura T, Pinker RT, Nakajima T (2011) Estimation of solar radiation using a neural network based on radiative transfer. *J Geophys Res* 116:D08215. <https://doi.org/10.1029/2009JD013337>
- Uchiyama A, Yamazaki A, Kudo R (2014) Column water vapor retrievals from sky radiometer (POM-02) 940 nm data. *J Meteorol Soc Jpn* 92A:195–203
- Uchiyama A, Matsunaga T, Yamazaki A (2018) The instrument constant of sky radiometers (POM-02)—Part 2: solid view angle. *Atmos Meas Tech* 11:5389–5402
- Uchiyama A, Shiobara M, Kobayashi H, Matsunaga T, Yamazaki A, Inei K, Kawai K, Watanabe Y (2019) Nocturnal aerosol optical depth measurements with modified sky radiometer POM-02 using the moon as a light source. *Atmos Meas Tech* 12:6465–6488. <https://doi.org/10.5194/amt-12-6465-2019>

Publisher's Note

Springer Nature remains neutral with regard to jurisdictional claims in published maps and institutional affiliations.

Submit your manuscript to a SpringerOpen[®] journal and benefit from:

- Convenient online submission
- Rigorous peer review
- Open access: articles freely available online
- High visibility within the field
- Retaining the copyright to your article

Submit your next manuscript at ► [springeropen.com](https://www.springeropen.com)
